ESAIM: M2AN 58 (2024) 1263–1299
https://doi.org/10.1051/m2an/2024035

ESAIM: Mathematical Modelling and Numerical Analysis
www.esaim-m2an.org

AN EXPLICIT WELL-BALANCED SCHEME ON STAGGERED GRIDS FOR BAROTROPIC EULER EQUATIONS

Thierry Goudon and Sebastian Minjeaud*

Abstract. In this paper, we introduce a specific modification of the numerical fluxes in order to insure the well-balanced property of schemes on staggered grids for the Euler equations. This property is crucial for the numerical representation of equilibrium solutions of balance laws with source terms, like when describing flows subjected to gravity and a complex topography. We propose first and second order versions of the well-balanced scheme. The performances of the method are evaluated through a series of 1D and 2D benchmarks.

Mathematics Subject Classification. 65M08, 76M12, 76NXX, 35Q31.

Received May 4, 2023. Accepted May 7, 2024.

1. Introduction

The motivation of this paper comes from the development of numerical strategies to compute the solutions of complex flows, by working on staggered grids. This means that the numerical unknowns are stored in different locations, depending on their type, in contrast to collocated approaches where the whole set of unknows is located at the same points.

Schemes on staggered grids are widely used for CFD applications in industrial context, in particular for applications in defence engineering, astrophysics, weather forecast or nuclear safety [1, 2, 7, 16, 68], Most of these hydrocodes relies on the Lagrangian framework, in the spirit of the pioneering schemes introduced in [65, 69], see the recent analysis in [22, 52]. Our work is concerned instead with Eulerian methods, in the spirit of [2, 10, 11, 30, 31, 43–45, 50, 59, 62, 64, 66, 67].

Staggered schemes are proven to be very efficient for the simulation of incompressible flows as illustrated by the celebrated MAC scheme [40]. Roughly speaking, the staggered discretizations allow to avoid the well-known spurious chessboard modes developed for incompressible flows when using collocated approaches. Their extensions to compressible flows trace back to [41]. It is expected that the use of staggered schemes for compressible flows might have some advantages when dealing with certain asymptotic regimes, like the low Mach regimes, or when some incompressibility-like constraint arises in the model. For instance, models for the simulation of mixture flows involve volume fractions and velocities for the carrier fluid and a disperse phase, and, since the sum of the volume fractions equals 1, a combination of the velocity fields of the two phases – the mean volume velocity – is divergence free; in turn, the model involves a pressure field associated to this constraint, see [12, 58]

Keywords and phrases. Finite volume schemes, staggered grids, well-balanced schemes, balance laws, shallow-Water.

Université Côte d'Azur, CNRS, Inria, LJAD, Parc Valrose, 06108 Nice, France.
*Corresponding author: Sebastian.MINJEAUD@unice.fr

and the references therein. To handle such models, with a reduced computational cost, a possible strategy is to use a time-splitting method enabling to uncouple the models for the two phases. The two systems to be solved are therefore closely related to the (single-phase) Euler (or Navier-Stokes) model and the constraint leads to the resolution of an additional elliptic problem for the pressure. The formulation of this elliptic problem at the discrete level in space appears to be more natural in the staggered framework (avoiding a decoupling between the unknowns located at the odd/even grids points), see [9, 12] for more details. Similarly, in low Mach regimes, working with collocated unknowns might lead to spurious instabilities, a difficulty that can be fixed by adopting dual discretizations. Moreover, it is now well established that collocated methods suffer from a lack of accuracy in low Mach number regimes [38, 39] and that some additional treatment, like preconditionning, are needed to restore their performances. Using staggered grids can be seen as an alternative viewpoint consisting in improving the performances of well established incompressible schemes to compressible low Mach regimes and fully compressible regimes [34, 42, 47, 59, 67]. This work is a contribution to this approach. A specific analysis has to be developed for such staggered schemes [11, 22, 29, 45, 46]. We have proposed staggered schemes with numerical fluxes inspired by the kinetic framework to discretize the (barotropic and full) Euler system, including second-order extensions [35] or considering unstructured grids [36]. The issues of low Mach number flows has been analysed in [34].

Here, we address the important issue of the treatment of *source terms* in such a staggered framework. Indeed, it is well-known that a direct discretization of the source terms, say for instance the gravity force, leads to inaccurate results, due to the inability to preserve steady state solutions. A classical illustration is the simulation of the Shallow-Water system with topography. The difficulty has been pointed out on the seminal papers [8, 17, 37] which have given raise to many progress in order to design suitable methods that can handle accurately the source terms, for scalar equations [14], and for systems [3–5, 18, 51]; we refer the reader to the detailed presentations in [15, 33]. The basic idea behind most of these methods is to modify the numerical fluxes by a hydrostatic reconstruction and to introduce a source discretization to balance the flux difference, compatible with the equilibrium state. We propose to adapt and analyse such strategies for schemes based on staggered discetizations for the barotropic Euler equations.

The paper is organized as follows. Section 2 explains how the source terms can be incorporated in the staggered mass and momentum fluxes. We detail the consistency analysis, the well-balanced property and we identify the stability condition that garanties the preservation of non negative densities. We also prove a semi-discrete entropy inequality. Next, we detail how the scheme can be modified in order to reach the second order accuracy, in the spirit of MUSCL procedures. Section 3 illustrates the abilities of the scheme in capturing equilibrium solutions, through a series of standard test cases in 1D and 2D.

2. Well-balanced scheme for the barotropic Euler system

2.1. Staggered scheme: notation and definitions

We consider the one-dimensional barotropic Euler system

$$\begin{cases} \partial_t \rho + \partial_x (\rho u) = 0, \\ \partial_t (\rho u) + \partial_x (\rho u \otimes u) + \partial_x (p(\rho)) = -\rho \partial_x z. \end{cases} \tag{1}$$

This model describes the evolution of a compressible fluid: the unknowns ρ and u stand respectively for the local density and velocity field of the fluid. They depend on the time and space variables, $t \geqslant 0$ and $x \in \mathbb{R}$. The pressure p depends on the density ρ only: we suppose that $\rho \mapsto p(\rho)$ belongs to $\mathcal{C}^1([0,\infty)) \cap \mathcal{C}^2(]0,\infty))$ and satisfies $p(0) = 0$, $p'(0) = 0$ and

$$p(\rho) > 0, \quad p'(\rho) > 0, \quad p''(\rho) \geqslant 0, \qquad \forall \rho > 0, \qquad \rho \longmapsto \frac{p(\rho)}{\rho^2} \in L^1_{\mathrm{loc}}([0,\infty)),$$

For instance, these properties hold for $p(\rho) = \kappa\rho^\gamma$ with $\kappa > 0$ and $\gamma > 1$. The force density function $x \mapsto z(x)$ is given. We refer the reader to the classical treatises [21,32,54,61] for a thorough introduction to these equations and for a description of the numerical issues. A case of particular interest is when $\gamma = 2$ (and $\kappa = 1/2$): the corresponding Shallow-Water system describes the free surface of a layer of fluid of constant density in hydrostatic balance, bounded from below by the bottom topography. In this case, ρ stands for the water depth, and z defines the bottom topography. In what follows, formula that apply to this specific case are distinguished by the tag (**SW**).

As said above, preserving numerically the equilibrium solutions is far from obvious. Here, we focus on the equilibrium states *at rest* that satisfy

$$u = 0, \qquad \partial_x p = -\rho \partial_x z.$$

Let us set

$$\mathscr{E}(\rho) = \frac{p(\rho)}{\rho} + \int_0^\rho \frac{p(s)}{s^2}\,\mathrm{d}s$$

(which is well-defined and positive for any $\rho > 0$, by virtue of the assumptions on the pressure law) so that

$$\mathscr{E}'(\rho) = \frac{p'(\rho)}{\rho}\cdot$$

In the specific case of the Shallow-Water system, we simply have

$$(\mathbf{SW}) \qquad p(\rho) = \frac{\rho^2}{2}, \qquad \mathscr{E}(\rho) = \rho.$$

In the general case, $\mathscr{E}$ is a strictly increasing function on $[0, \infty[$ with $\mathscr{E}(0) = 0$. Thus, it is a one-to-one function from $[0, \infty[$ to its range and we denote by $\mathscr{E}^{-1}$ the inverse function of $\mathscr{E}$.

Therefore, with the function $\mathscr{E}$ at hand, we readily see that, out of vacuum or dry areas ($\rho = 0$), the equilibrium satisfy

$$\mathscr{E}(\rho) + z = \textit{constant}.$$

By analogy with the case of Shallow-Water equations, this form of equilibrium is referred to as a flat water level. In fact, we aim at preserving a more general class of equilibrium which combine dry shore ($\rho = 0$) and flat water level ($\mathscr{E}(\rho) + z = \textit{constant}$), which amounts to impose

$$\mathscr{E}(\rho) + z = \max(\eta, z) \quad \text{with } \eta \text{ a constant.}$$

In areas where the bottom is lower than the level given by the constant η, the water level is flat whereas the area is dry when the bottom is higher than the level prescribed by η.

We address the issue of preserving equilibrium in the framework of staggered grids, with numerical densities and velocities stored in different locations. According to Figure 1,

- we introduce a set of $J+1$ points $x_1 = 0 < x_2 < ... < x_J < x_{J+1} = L$ in the computational domain; we denote by $\mathcal{C}_{j+\frac12} = [x_j, x_{j+1}]$, $j \in [\![1, J]\!]$, the cells defined by these points;
- we denote by $x_{j+\frac12} = (x_j + x_{j+1})/2$, $j \in [\![1, J]\!]$, the centers of the cells; these points define the dual cells $\mathcal{C}_j = [x_{j-\frac12}, x_{j+\frac12}]$, $j \in [\![2, J]\!]$;
- we set the following notation for the mesh-sizes

$$\delta x_{j+\frac12} = x_{j+1} - x_j, \ j \in [\![1, J]\!], \quad \text{and} \quad \delta x_j = \frac{\delta x_{j-\frac12} + \delta x_{j+\frac12}}{2}, \ j \in [\![2, J]\!],$$

(with the specific definition for the end-cells: $\delta x_1 = \frac12 \delta x_{\frac32}$ and $\delta x_{J+1} = \frac12 \delta x_{J+\frac12}$). The discrete densities $\rho_{j+\frac12}$ are thought of as approximation of the density ρ on the cells $\mathcal{C}_{j+\frac12}$ whereas the discrete velocities u_j are thought of as approximation of the velocity u on the cells $\mathcal{C}_j$. Here and below, we denote

$$\delta x = \max\left\{\delta x_j, \delta x_{j+\frac12}, \ j \in \{1, ...J\}\right\}.$$

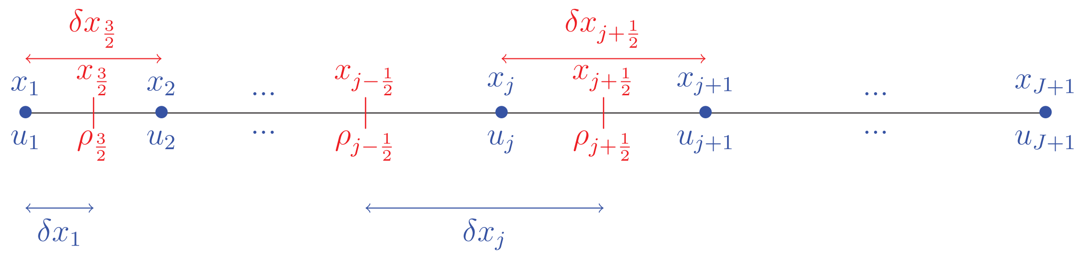

FIGURE 1. Staggered grid in dimension one.

Throughout the paper we shall use the notation

$$[z]_+ = \max(0, z) \geqslant 0, \qquad [z]_- = \min(0, z) \leqslant 0.$$

In what follows, we denote $(\hat{u}_j, \hat{\rho}_{j+\frac{1}{2}})$ a discrete equilibrium at rest with possibly a dry area, thus characterized by

$$\hat{u}_j = 0, \qquad \mathscr{E}(\hat{\rho}_{j+\frac{1}{2}}) + z_{j+\frac{1}{2}} = \max\left(\eta, z_{j+\frac{1}{2}}\right). \tag{2}$$

where $\eta \in \mathbb{R}$ is a given constant. We address the question of the conservation of such an equilibrium by the numerical scheme.

With these notations, we update the numerical unknowns, having at hand the $\rho_{j+1/2}$'s and the u_j's, by

$$\frac{\overline{\rho}_{j+\frac{1}{2}} - \rho_{j+\frac{1}{2}}}{\delta t} + \frac{\mathcal{F}_{j+1} - \mathcal{F}_j}{\delta x_{j+\frac{1}{2}}} = 0, \tag{3}$$

$$\frac{\overline{\rho}_j \overline{u}_j - \rho_j u_j}{\delta t} + \frac{\mathcal{G}_{j+\frac{1}{2}} - \mathcal{G}_{j-\frac{1}{2}}}{\delta x_j} + \frac{\Pi_{j+\frac{1}{2}} - \Pi_{j-\frac{1}{2}}}{\delta x_j} = -S_j, \tag{4}$$

where the overlined quantities $\overline{\rho}_{j+\frac{1}{2}}$, $\overline{\rho}_j \overline{u}_j$ denotes the updated numerical unknowns and ρ_j is an averaged quantity on the cell $\mathcal{C}_j$ (see (9) below). These discrete formula are intended to mimic the integration of the mass conservation equation over $[n\delta t, (n+1)\delta t] \times \mathcal{C}_{j+\frac{1}{2}}$ and of the momentum balance over $[n\delta t, (n+1)\delta t] \times \mathcal{C}_j$: the details of the numerical methods depend on the design of the numerical fluxes $\mathcal{F}_j, \mathcal{G}_{j+\frac{1}{2}}, \Pi_{j+\frac{1}{2}}$ on the interfaces of the control volumes.

Let us start by presenting the construction of the scheme in the source-free case; we will discuss why and how it can be modified in order to account for the presence of source terms. The construction uses the values of the unknowns stored on the interface and in the neighbouring cells. Namely, our study is motivated by the scheme defined in [11, 12, 35]: taking into account the characteristic speeds of the system

$$\lambda_\pm(\rho, u) = u \pm c(\rho), \qquad c(\rho) = \sqrt{p'(\rho)},$$

we adopt the following definition that relies on the UpWinding principles,

$$\mathcal{F}_j = \mathcal{F}_j^+ + \mathcal{F}_j^-,$$

with

$$\mathcal{F}_j^+ = \mathcal{F}^+(\rho_{j-\frac{1}{2}}, u_j) \quad \text{and} \quad \mathcal{F}_j^- = \mathcal{F}^-(\rho_{j+\frac{1}{2}}, u_j). \tag{5}$$

The flux functions $\mathcal{F}^\pm$ are given by

$$\mathcal{F}^+(\rho, u) = \begin{cases} 0 & \text{if } u \leqslant -c(\rho), \\ \dfrac{\rho}{4c(\rho)}(u + c(\rho))^2 & \text{if } |u| \leqslant c(\rho), \\ \rho u & \text{if } u \geqslant c(\rho), \end{cases} \tag{6}$$

and

$$\mathcal{F}^-(\rho,u) = \begin{cases} \rho u & \text{if } u \leqslant -c(\rho), \\ -\dfrac{\rho}{4c(\rho)}(u-c(\rho))^2 & \text{if } |u| \leqslant c(\rho), \\ 0 & \text{if } u \geqslant c(\rho). \end{cases} \tag{7}$$

This simple formula is inspired from the kinetic schemes [20, 25, 26, 49, 56, 57] since it comes from

$$\mathcal{F}^\pm(\rho,u) = \int_{\pm\xi>0} M_{\rho,u}(\xi)\,\mathrm{d}\xi,$$

where $M_{\rho,u}$ is the "Maxwellian state"

$$M_{\rho,u}(\xi) = \frac{1}{2c(\rho)}\mathbf{1}_{|\xi-u|\leq c(\rho)}.$$

An alternative definition of the numerical fluxes can be obtained by using the Dirac mass centred on the material velocity: $M_{\rho,u}(\xi) = \delta(\xi = u)$; this gives the scheme introduced in [44]. As a matter of fact, the flux function satisfy the symmetry property

$$\mathcal{F}^-(\rho,u) = -\mathcal{F}^+(\rho,-u),$$

and the flux–consistency condition

$$\mathcal{F}^+(\rho,u) + \mathcal{F}^-(\rho,u) = \rho u. \tag{8}$$

For stability analysis, it is important to observe that

$$\rho \longmapsto \pm\mathcal{F}^\pm(\rho,u) \text{ are non-decreasing functions.}$$

We turn to the momentum balance. We start by setting

$$\rho_j = \frac{\delta x_{j+\frac12}\rho_{j+\frac12} + \delta x_{j-\frac12}\rho_{j-\frac12}}{2\delta x_j}, \tag{9}$$

and

$$\mathcal{F}^\pm_{j+\frac12} = \frac{\mathcal{F}^\pm_j + \mathcal{F}^\pm_{j+1}}{2}, \qquad \mathcal{F}_{j+\frac12} = \mathcal{F}^+_{j+\frac12} + \mathcal{F}^-_{j+\frac12}. \tag{10}$$

Remarkably, the conservation relation

$$\overline{\rho}_j - \rho_j + \frac{\delta t}{\delta x_j}(\mathcal{F}_{j+\frac12} - \mathcal{F}_{j-\frac12}) = 0 \tag{11}$$

holds.

Indeed, we are led to compute

$$\frac{\delta x_{j+\frac12}}{2\delta x_j}\frac{\mathcal{F}_{j+1}-\mathcal{F}_j}{\delta x_{j+\frac12}} + \frac{\delta x_{j-\frac12}}{2\delta x_j}\frac{\mathcal{F}_j-\mathcal{F}_{j-1}}{\delta x_{j-\frac12}} = \frac{\mathcal{F}_{j+1}-\mathcal{F}_{j-1}}{2\delta x_j} = \frac{\mathcal{F}_{j+\frac12}-\mathcal{F}_{j-\frac12}}{\delta x_j}.$$

The convection fluxes are obtained by applying the UpWinding principle, based on the "sign" of the mass fluxes $\mathcal{F}_j$ and $\mathcal{F}_{j+1}$, to the velocity field; we set

$$\mathcal{G}_{j+\frac12} = u_j\mathcal{F}^+_{j+\frac12} + u_{j+1}\mathcal{F}^-_{j+\frac12}. \tag{12}$$

(The scheme designed in [44] adopts a different averaged definition for obtaining the momentum fluxes from the mass fluxes.) Finally, the pressure gradient at $x_{j+\frac12}$ is naturally centred

$$\Pi_{j+\frac12} = p(\rho_{j+\frac12}). \tag{13}$$

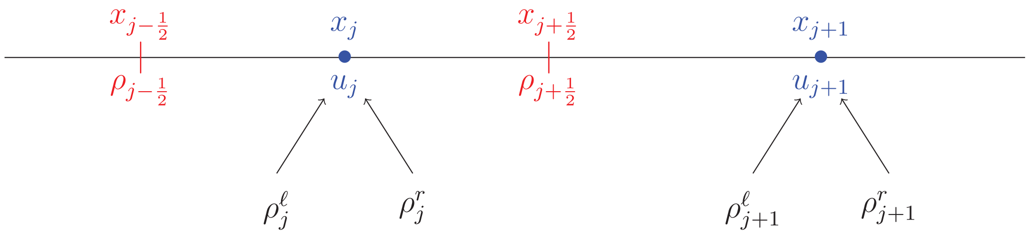

FIGURE 2. Reconstruction of a WB density.

Owing to (8), the momentum flux is consistent. Without source terms, the scheme can be shown to preserve the positivity of the density and the entropy dissipation property under a suitable CFL condition [11], it is thus consistent with the Euler system [10]. For the source term, a natural approach consists in setting

$$S_j = \rho_j \frac{z_{j+\frac{1}{2}} - z_{j-\frac{1}{2}}}{\delta x_j}.$$

It looks a reasonable choice: at least, the consistency analysis plugging into this expression the continuous equilibrium solution produces an error term of order $\mathscr{O}(\delta x_j)$. Unfortunately this definition does not produce satisfactory results, since it does not preserve the discrete equilibrium solution: while $\mathscr{E}(\hat\rho_{j+\frac{1}{2}}) + z_{j+\frac{1}{2}} = \mathscr{E}(\hat\rho_{j-\frac{1}{2}}) + z_{j-\frac{1}{2}}$, in general $p(\hat\rho_{j+\frac{1}{2}}) - p(\hat\rho_{j-\frac{1}{2}}) + \hat\rho_j(z_{j+\frac{1}{2}} - z_{j-\frac{1}{2}})$ does not vanish. Hence, the equilibrium is poorly captured, with spurious non zero velocities, see for instance the comments in [12]. (We refer the reader to Remark 2.2 for further comments, describing a specific situation – for the Shallow-Water equation and the fluxes of [44] – where such a definition is well-balanced, though.)

2.2. Incorporation of the source terms

According to [14] and [3–5, 15], we introduce hydrostatic reconstructions of the density, compatible with the equilibrium, defined at the interfaces x_j (see Fig. 2) by setting

$$z_j = \max(z_{j+\frac{1}{2}}, z_{j-\frac{1}{2}}), \tag{14}$$

$$\mathscr{E}(\rho_j^r) = \big[\mathscr{E}(\rho_{j+\frac{1}{2}}) + z_{j+\frac{1}{2}} - z_j\big]_+, \tag{15}$$

$$\mathscr{E}(\rho_j^\ell) = \big[\mathscr{E}(\rho_{j-\frac{1}{2}}) + z_{j-\frac{1}{2}} - z_j\big]_+. \tag{16}$$

It is important to note that, as proved in the sequel, these two reconstructions ρ_j^r and ρ_j^ℓ are equal if the system is at an equilibrium state. Accordingly, it allows us to exactly preserve equilibrium states when proceeding as follows. With these quantities ρ_j^ℓ and ρ_j^r at hand, we replace the definition of the mass flux in (5) by

$$\mathcal{F}_j^+ = \mathcal{F}^+(\rho_j^\ell, u_j) \quad \text{and} \quad \mathcal{F}_j^- = \mathcal{F}^-(\rho_j^r, u_j),$$

which still accounts for the UpWinding principles. For the momentum, we proceed as follows:

- the convection fluxes are defined with these reconstructed mass fluxes, by using (10) and (12),
- the pressure gradient uses the centered definition based on the reconstructed densities

$$p(\rho_j^r) - p(\rho_j^\ell).$$

The non-conservative source term is embodied in this definition.

Thus, we introduce the following mass fluxes, momentum convection fluxes, and the source term

$$
\begin{aligned}
\mathscr{F}_j &= \mathcal{F}^+(\rho_j^\ell, u_j) + \mathcal{F}^-(\rho_j^r, u_j),\\
\mathscr{G}_{j+\frac12} &= \frac{u_j}{2}\Big(\mathcal{F}^+(\rho_j^\ell, u_j) + \mathcal{F}^+(\rho_{j+1}^\ell, u_{j+1})\Big) + \frac{u_{j+1}}{2}\Big(\mathcal{F}^-(\rho_j^r, u_j) + \mathcal{F}^-(\rho_{j+1}^r, u_{j+1})\Big),\\
S_j &= p(\rho_j^r) - p(\rho_{j+\frac12}) - p(\rho_j^\ell) + p(\rho_{j-\frac12}).
\end{aligned}
\tag{17}
$$

The well-balanced scheme reads

$$
\begin{aligned}
\overline{\rho}_{j+\frac12} &= \rho_{j+\frac12} - \frac{\delta t}{\delta x_{j+\frac12}}\Big(\mathscr{F}_{j+1} - \mathscr{F}_j\Big),\\
\overline{\rho}_j\overline{u}_j &= \rho_j u_j - \frac{\delta t}{\delta x_j}\bigg(\Big(\mathscr{G}_{j+\frac12} + \Pi_{j+\frac12}\Big) - \Big(\mathscr{G}_{j-\frac12} + \Pi_{j-\frac12}\Big) + S_j\bigg),
\end{aligned}
\tag{18}
$$

with $\Pi_{j+\frac12} = p(\rho_{j+\frac12})$.

Consistency. The consistency with the exact fluxes comes directly from the consistency of $\mathcal{F}_j$ and $\mathcal{G}_{j+\frac12}$. Indeed, if $z_{j-\frac12} = z_{j+\frac12} = z_{j+\frac32}$ then we have $\rho_j^r = \rho_{j+\frac12}$, $\rho_j^\ell = \rho_{j-\frac12}$ and $\rho_{j+1}^r = \rho_{j+\frac32}$, $\rho_{j+1}^\ell = \rho_{j+\frac12}$, so that, in this case, $\mathscr{F}_j = \mathcal{F}_j$ and $\mathscr{G}_{j+\frac12} = \mathcal{G}_{j+\frac12}$. The flux-consistency is thus a consequence of (8). More interestingly, $S_j/\delta x_j$ is consistent with the source term $\rho\partial_x z$. Let us denote by δz_j the quantity $z_{j+\frac12} - z_{j-\frac12}$. If z is a regular function this quantity is of order δx_j. We first investigate the specific case of the Shallow-Water system far from dry/wet transition (more precisely assuming that $\min\big(\rho_{j-\frac12}, \rho_{j+\frac12}\big) \geqslant |\delta z_j|$ holds). We get

$$
(\mathbf{SW})\qquad S_j = \frac12(\rho_j^r - \rho_{j+\frac12})(\rho_j^r + \rho_{j+\frac12}) - \frac12(\rho_j^\ell - \rho_{j-\frac12})(\rho_j^\ell + \rho_{j-\frac12})
$$

where the equilibrium relations cast as

$$
(\mathbf{SW})\qquad \rho_j^r = \rho_{j+\frac12} - \big[\delta z_j\big]_-, \qquad \rho_j^\ell = \rho_{j-\frac12} - \big[\delta z_j\big]_+.
$$

Hence, we obtain

$$
(\mathbf{SW})\qquad S_j = \frac{\rho_{j+\frac12} + \rho_{j-\frac12}}{2}\delta z_j - \frac{\rho_j^r - \rho_j^\ell}{2}|\delta z_j|. \tag{19}
$$

It follows that S_j is (first order) consistent with $\rho\partial_x z$. In the general case, the consistency with the source term comes from the following expansion. As for the case of Shallow-Water equations, the expression of ρ_j^r and ρ_j^ℓ depends on the sign of δz_j. If $\delta z_j \geqslant 0$, we have the exact equality $\rho_j^r = \rho_{j+\frac12}$. But, if $\delta z_j \leqslant 0$, we have $\rho_j^r = \mathscr{E}^{-1}([\mathscr{E}(\rho_{j+\frac12}) + \delta z_j]_+)$. Thus, when $\delta z_j \leqslant 0$, in the case where $\mathscr{E}(\rho_{j+\frac12}) \leqslant -\delta z_j$, we have $\rho_j^r = 0$ whereas, in the case where $\mathscr{E}(\rho_{j+\frac12}) \geqslant -\delta z_j$, a Taylor expansion leads to

$$
\rho_j^r = \rho_{j+\frac12} + \delta z_j \frac{\rho_{j+\frac12}}{p'(\rho_{j+\frac12})} + o(|\delta z_j|), \qquad (\text{when } \delta z_j \leqslant 0 \text{ and } \mathscr{E}(\rho_{j+\frac12}) \geqslant \delta z_j),
$$

since $\Big(\mathscr{E}^{-1}\Big)'\big(\mathscr{E}(\rho)\big) = \dfrac{\rho}{p'(\rho)}$. Finally, we have

$$
\rho_j^r = \begin{cases}
0, & \text{if } \delta z_j \leqslant 0 \text{ and } \mathscr{E}(\rho_{j+\frac12}) \leqslant |\delta z_j|,\\
\rho_{j+\frac12} + \delta z_j \dfrac{\rho_{j+\frac12}}{p'(\rho_{j+\frac12})} + o(|\delta z_j|), & \text{if } \delta z_j \leqslant 0 \text{ and } \mathscr{E}(\rho_{j+\frac12}) \geqslant |\delta z_j|,\\
\rho_{j+\frac12}, & \text{if } \delta z_j \geqslant 0,
\end{cases}
\tag{20}
$$

and, similarly,

$$\rho_j^\ell = \begin{cases} \rho_{j-\frac12}, & \text{if } \delta z_j \leqslant 0, \\ \rho_{j-\frac12} - \delta z_j \dfrac{\rho_{j-\frac12}}{p'(\rho_{j-\frac12})} + o(|\delta z_j|), & \text{if } \delta z_j \geqslant 0 \text{ and } \mathscr{E}(\rho_{j-\frac12}) \geqslant |\delta z_j|, \\ 0, & \text{if } \delta z_j \geqslant 0 \text{ and } \mathscr{E}(\rho_{j-\frac12}) \leqslant |\delta z_j|. \end{cases} \tag{21}$$

Following the same lines, since

$$\Big(p\circ\mathscr{E}^{-1}\Big)'(\mathscr{E}(\rho)) = \rho \quad \text{and} \quad \Big(p\circ\mathscr{E}^{-1}\Big)''(\mathscr{E}(\rho)) = \frac{\rho}{p'(\rho)},$$

we have the following expressions for $p(\rho_j^r)$ and $p(\rho_j^\ell)$

$$p(\rho_j^r) = \begin{cases} 0, & \text{if } \delta z_j \leqslant 0 \text{ and } \mathscr{E}(\rho_{j+\frac12}) \leqslant |\delta z_j|, \\ p(\rho_{j+\frac12}) + \delta z_j \rho_{j+\frac12} + \dfrac{\delta z_j^2}{2}\dfrac{\rho_{j+\frac12}}{p'(\rho_{j+\frac12})} + o(|\delta z_j|^2), & \text{if } \delta z_j \leqslant 0 \text{ and } \mathscr{E}(\rho_{j+\frac12}) \geqslant |\delta z_j|, \\ p(\rho_{j+\frac12}), & \text{if } \delta z_j \geqslant 0, \end{cases} \tag{22}$$

and

$$p(\rho_j^\ell) = \begin{cases} p(\rho_{j-\frac12}), & \text{if } \delta z_j \leqslant 0, \\ p(\rho_{j-\frac12}) - \delta z_j \rho_{j-\frac12} + \dfrac{\delta z_j^2}{2}\dfrac{\rho_{j-\frac12}}{p'(\rho_{j-\frac12})} + o(|\delta z_j|^2), & \text{if } \delta z_j \geqslant 0 \text{ and } \mathscr{E}(\rho_{j-\frac12}) \geqslant |\delta z_j|, \\ 0, & \text{if } \delta z_j \geqslant 0 \text{ and } \mathscr{E}(\rho_{j-\frac12}) \leqslant |\delta z_j|. \end{cases} \tag{23}$$

We observe that the case where $p(\rho_j^r) = 0$ occurs only when $\rho_{j+\frac12}$ is sufficiently small since, in this case, $\rho_{j+\frac12} \leqslant \mathscr{E}^{-1}(|\delta z_j|) \underset{\delta x\to 0}{\longrightarrow} 0$. Moreover, an expansion of $p(\rho_{j+\frac12})$ in this case shows that

$$\begin{aligned} p(\rho_{j+\frac12}) &= p\circ\mathscr{E}^{-1}\big(\mathscr{E}(\rho_{j+\frac12})\big) \\ &= p\circ\mathscr{E}^{-1}(0) + \Big(p\circ\mathscr{E}^{-1}\Big)'(0)\ \mathscr{E}(\rho_{j+\frac12}) + o(|\mathscr{E}(\rho_{j+\frac12})|) \\ &= o(|\mathscr{E}(\rho_{j+\frac12})|). \end{aligned} \tag{24}$$

This proves that, in the case where $\mathscr{E}(\rho_{j+\frac12}) \leqslant |\delta z_j|$, we have

$$p(\rho_{j+\frac12}) + \delta z_j \rho_{j+\frac12} = o(|\delta z_j|).$$

Thus, we finally have

$$p(\rho_j^r) = \begin{cases} p(\rho_{j+\frac12}) + \delta z_j \rho_{j+\frac12} + o(|\delta z_j|), & \text{if } \delta z_j \leqslant 0, \\ p(\rho_{j+\frac12}), & \text{if } \delta z_j \geqslant 0, \end{cases}$$

and similarly

$$p(\rho_j^\ell) = \begin{cases} p(\rho_{j-\frac12}), & \text{if } \delta z_j \leqslant 0, \\ p(\rho_{j-\frac12}) - \delta z_j \rho_{j-\frac12} + o(|\delta z_j|), & \text{if } \delta z_j \geqslant 0, \end{cases}$$

It leads to the following equality for S_j

$$S_j = \begin{cases} \delta z_j \rho_{j+\frac12} + o(|\delta z_j|), \text{ if } \delta z_j \leqslant 0, \\ \delta z_j \rho_{j-\frac12} + o(|\delta z_j|), \text{ if } \delta z_j \geqslant 0. \end{cases}$$

The term $S_j/\delta x_j$ is thus consistent with $\rho\partial_x z$.

Remark 2.1. Far from wet/dry transition (when $\min(\mathscr{E}(\rho_{j-\frac{1}{2}}), \mathscr{E}(\rho_{j+\frac{1}{2}})) \geqslant |\delta z_j|$) a first order consistency error is obtained. Moreover, it also applies in dry area if $\lim_{\rho\to 0} p''(\rho) \neq 0$ since in this case, the $o(|\mathscr{E}(\rho_{j+\frac{1}{2}})|)$ in (24) is actually a $O(|\mathscr{E}(\rho_{j+\frac{1}{2}})|^2)$.

Preservation of equilibrium state. A key property of the construction is the equality $\rho_j^r = \rho_j^\ell$ at equilibrium. Indeed, by definition of the equilibrium state (2) associated to the constant η, we have

$$\mathscr{E}(\rho_{j\pm\frac{1}{2}}) + z_{j\pm\frac{1}{2}} = \max\left(z_{j\pm\frac{1}{2}}, \eta\right),$$

so that, since $z_j = \max(z_{j-\frac{1}{2}}, z_{j+\frac{1}{2}})$, at the equilibrium state we have

$$\mathscr{E}(\rho_j^r) = \mathscr{E}(\rho_j^\ell) \quad = [\eta - z_j]_+.$$

It ensures the equality $\rho_j^r = \rho_j^\ell$. Note that the positive part in the definiton (14) of ρ_j^r and ρ_j^ℓ is crucial to ensure the equality $\rho_j^r = \rho_j^\ell$ in the dry area (where $z_j > \eta$).

Thus, if the system is at an equilibrium state, that is, in particular, $\rho_{j-\frac{1}{2}} = \hat{\rho}_{j-\frac{1}{2}}$, $\rho_{j+\frac{1}{2}} = \hat{\rho}_{j+\frac{1}{2}}$, $\rho_{j+\frac{3}{2}} = \hat{\rho}_{j+\frac{3}{2}}$, $u_j = 0$, $u_{j-1} = 0$ and $u_{j+1} = 0$, as mentionned above, we have $\rho_j^r = \rho_j^\ell$ and $\rho_{j+1}^r = \rho_{j+1}^\ell$. Thus, the mass fluxes vanish at $x_{j+\frac{1}{2}}$ and $x_{j-\frac{1}{2}}$ since, by consistency of the splitting, they are equal to $\rho_{j+1}^r u_{j+1} = \rho_{j+1}^\ell u_{j+1} = 0$ and $\rho_j^r u_j = \rho_j^\ell u_j = 0$ respectively. The density remains unchanged. Since $u_j = 0$, $u_{j-1} = 0$ and $u_{j+1} = 0$, the momentum fluxes vanish and the sum of the pressure and source term which is equal to $p(\rho_j^r) - p(\rho_j^\ell)$ is also zero since $\rho_j^r = \rho_j^\ell$. The velocity remains unchanged and the equilibrium states are perfectly preserved.

Remark 2.2 (A simple staggered WB scheme for the Shallow-Water system, [27])**.** For the Shallow-Water system, the following simple staggered scheme, proposed in [27], based on the UpWinding according to the material velocity as in [44]

$$\begin{aligned}
\overline{\rho}_{j+\frac{1}{2}} &= \rho_{j+\frac{1}{2}} - \frac{\delta t}{\delta x_{j+\frac{1}{2}}} \underbrace{\left([u_{j+1}]_+ \rho_{j+\frac{1}{2}} + [u_{j+1}]_- \rho_{j+\frac{3}{2}}\right)}_{\mathcal{F}_{j+1}} \Big) \\
&\qquad\qquad - \frac{\delta t}{\delta x_{j+\frac{1}{2}}} \underbrace{\left([u_j]_+ \rho_{j-\frac{1}{2}} + [u_j]_- \rho_{j+\frac{1}{2}}\right)}_{\mathcal{F}_j}, \\
\overline{\rho}_j \overline{u}_j &= \rho_j u_j - \frac{\delta t}{2\delta x_j}\Big(u_j[\mathcal{F}_j + \mathcal{F}_{j+1}]_+ + u_{j+1}[\mathcal{F}_j + \mathcal{F}_{j+1}]_-\Big) \\
&\quad - \frac{\delta t}{2\delta x_j}\Big(u_{j-1}[\mathcal{F}_{j-1} + \mathcal{F}_j]_+ + u_j[\mathcal{F}_{j-1} + \mathcal{F}_j]_-\Big) \\
&\quad - \frac{\delta t}{\delta x_j}(p(\rho_{j+\frac{1}{2}}) - p(\rho_{j-\frac{1}{2}})) - \frac{\delta t}{\delta x_j}(\rho_{j+\frac{1}{2}} + \rho_{j-\frac{1}{2}})\frac{z_{j+\frac{1}{2}} - z_{j-\frac{1}{2}}}{2}
\end{aligned} \tag{25}$$

is well-balanced in the case where there is no dry area. If $(\hat{\rho}_{j+\frac{1}{2}}, \hat{u}_j)$ is an equilibrium state with no dry area (see (2) with $\eta > \max_j\left(z_{j+\frac{1}{2}}\right)$), the mass fluxes and the convection fluxes vanish since $\hat{u}_j = 0$, while the last two terms of the momentum equation in (25) recombine as $\frac{\hat{\rho}_{j+\frac{1}{2}} + \hat{\rho}_{j-\frac{1}{2}}}{2}\left((\hat{\rho}_{j+\frac{1}{2}} + z_{j+\frac{1}{2}}) - (\hat{\rho}_{j-\frac{1}{2}} + z_{j-\frac{1}{2}})\right)$. Away from wet/dry transition, this term vanishes too. Note that the well-balanced property of the scheme (25) in this case crucially relies on the specific form of both the numerical fluxes and of the pressure law.

Preservation of density positivity. The numerical scheme should at least preserve the positivity of the density, which can be seen as a minimal stability criterion. To this end, we observe that $\rho \mapsto \mathscr{E}(\rho)$ is non-decreasing. Hence, since $z_j \geqslant z_{j\pm\frac{1}{2}}$, we have $\mathscr{E}(\rho_{j+1}^\ell) \leqslant \mathscr{E}(\rho_{j+\frac{1}{2}})$, $\mathscr{E}(\rho_j^r) \leqslant \mathscr{E}(\rho_{j+\frac{1}{2}})$ and thus $\rho_{j+1}^\ell \leqslant \rho_{j+\frac{1}{2}}$,

$\rho_j^r \leqslant \rho_{j+\frac{1}{2}}$. The monotonicity of the flux function leads to $\mathcal{F}^+(\rho_{j+1}^\ell, u_{j+1}) \leqslant \mathcal{F}^+(\rho_{j+\frac{1}{2}}, u_{j+1})$ and $\mathcal{F}^-(\rho_j^r, u_j) \geqslant \mathcal{F}^-(\rho_{j+\frac{1}{2}}, u_j)$. Since $\mathcal{F}^+(\rho_j^\ell, u_j) \geqslant 0$ and $-\mathcal{F}^-(\rho_{j+1}^r, u_{j+1}) \geqslant 0$, we arrive from (18) at

$$\begin{aligned}\overline{\rho}_{j+\frac{1}{2}} &\geqslant \rho_{j+\frac{1}{2}} - \frac{\delta t}{\delta x_{j+\frac{1}{2}}}\mathcal{F}^+(\rho_{j+1}^\ell, u_{j+1}) + \frac{\delta t}{\delta x_{j+\frac{1}{2}}}\mathcal{F}^-(\rho_j^r, u_j)\\ &\geqslant \rho_{j+\frac{1}{2}} - \frac{\delta t}{\delta x_{j+\frac{1}{2}}}\mathcal{F}^+(\rho_{j+\frac{1}{2}}, u_{j+1}) + \frac{\delta t}{\delta x_{j+\frac{1}{2}}}\mathcal{F}^-(\rho_{j+\frac{1}{2}}, u_j).\end{aligned}$$

We can now conclude as in Proposition 3.7 of [11]: under the CFL-condition

$$\frac{\delta t}{\delta x_{j+\frac{1}{2}}}\Big(\big[\lambda_+(\rho_{j+\frac{1}{2}}, u_{j+1})\big]_+ + \big[\lambda_-(\rho_{j+\frac{1}{2}}, u_j)\big]_-\Big) \leqslant 1$$

the scheme (18) preserves the positivity of the discrete density.

Entropy inequality. We prove an entropy inequality for a semi-discrete version of the scheme: the time t is kept as a continuous variable and only the space variable is discretized. We use the same notation as above, except that the quantities $\rho_{j+\frac{1}{2}}$, u_j and, consequently, ρ_j, ρ_j^r, ρ_j^ℓ, *etc*, are here considered as functions of the continuous time variable t. The hydrostatic resconstructions are still defined by (14). The fluxes are defined by (17). However, the scheme (18) is replaced by its semi-discrete version:

$$\begin{aligned}\frac{\mathrm{d}\rho_{j+\frac{1}{2}}}{\mathrm{d}t}(t) &= -\frac{1}{\delta x_{j+\frac{1}{2}}}\Big(\mathscr{F}_{j+1} - \mathscr{F}_j\Big),\\ \frac{\mathrm{d}(\rho_j u_j)}{\mathrm{d}t}(t) &= -\frac{1}{\delta x_j}\Big(\mathscr{G}_{j+\frac{1}{2}} - \mathscr{G}_{j-\frac{1}{2}} + p(\rho_j^r) - p(\rho_j^\ell)\Big),\end{aligned} \tag{26}$$

where the mean density ρ_j is defined by (9).

We denote by Φ the function of class $\mathcal{C}^2(]0,\infty[)$ such that

$$\rho\Phi'(\rho) - \Phi(\rho) = p(\rho), \forall \rho > 0.$$

The function Φ stands for the internal energy. For smooth solutions, multiplying the first equation of (1) by $\Phi'(\rho) + z$ leads to

$$\partial_t\big[\Phi(\rho) + \rho z\big] + \partial_x\Big[\big(\Phi(\rho) + \rho z\big)u\Big] + p(\rho)\partial_x u - \rho u \partial_x z = 0. \tag{27}$$

This is the internal and potential energy balance equation for system (1). Similarly, for smooth solutions, the kinetic energy balance equation is obtained by multiplying the second equation of (1) by u and substracting the vanishing term $u^2/2 \times \big[\partial_t \rho + \partial_x(\rho u)\big]$:

$$\partial_t\Big[\rho\frac{u^2}{2}\Big] + \partial_x\Big[\rho\frac{u^2}{2}u\Big] + u\partial_x\big(p(\rho)\big) + \rho u \partial_x z = 0. \tag{28}$$

Adding the two balance laws (27) and (28) leads to the following "conservative" entropy inequality

$$\partial_t\Big[\rho\frac{u^2}{2} + \Phi(\rho) + \rho z\Big] + \partial_x\Big[\Big(\rho\frac{u^2}{2} + \Phi(\rho) + \rho z + p(\rho)\Big)u\Big] \leqslant 0. \tag{29}$$

Inequality holds when the solutions become discontinous. We aim at establishing a semi-discrete version of this inequality.

The first step relies on Lemma 4.4 in Appendix A of [11]. This is the result that allows us to prove the discrete internal energy balance law in the absence of source term. Taking the parameters λ, μ go to the infinity in this statement, we obtain

$$\Big[\Phi(\rho_2) - \Phi(\rho_1)\Big] V - \Phi'(\rho_2)\Big[\mathcal{F}^+(\rho_2, V) - \mathcal{F}^+(\rho_1, V)\Big] - \Phi'(\rho_1)\Big[\mathcal{F}^-(\rho_2, V) - \mathcal{F}^-(\rho_1, V)\Big] \leqslant 0, \quad \forall \rho_1 > 0, \forall \rho_2 > 0, \forall V \in \mathbb{R}.$$

Using the notation $\mathcal{F}(\rho_1, \rho_2, V) = \mathcal{F}^+(\rho_1, V) + \mathcal{F}^-(\rho_2, V)$ and the definition of Φ, this relation can be written, for all $\rho_1,\ \rho_2 > 0$ and for all $V \in \mathbb{R}$

$$-p(\rho_2)V + \Phi'(\rho_2)\mathcal{F}(\rho_1, \rho_2, V) \leqslant -p(\rho_1)V + \Phi'(\rho_1)\mathcal{F}(\rho_1, \rho_2, V). \tag{30}$$

Let us now consider $\rho_1 > 0$, $\rho_2 > 0$, $z_1 \in \mathbb{R}$, $z_2 \in \mathbb{R}$ and $V \in \mathbb{R}$. We define the two quantities ρ_1^* and ρ_2^* (which stands for the hydrostatic equilibriums built from ρ_1, ρ_2, z_1, z_2)

$$\mathscr{E}(\rho_1^*) = \Big[\mathscr{E}(\rho_1) + z_1 - z^*\Big]_+ \quad \text{and} \quad \mathscr{E}(\rho_2^*) = \Big[\mathscr{E}(\rho_2) + z_2 - z^*\Big]_+,$$

with $z^* = \max(z_1, z_2)$. We aim at proving

$$-p(\rho_2^*)V + \Big[\Phi'(\rho_2) + z_2\Big]\mathcal{F}(\rho_1^*, \rho_2^*, V) \leqslant -p(\rho_1^*)V + \Big[\Phi'(\rho_1) + z_1\Big]\mathcal{F}(\rho_1^*, \rho_2^*, V). \tag{31}$$

This is the analog of the result stated in Lemma 4.4 in Appendix A of [11], taking into account the source term and the well balanced scheme. To prove this result (see [15]) we first apply (30) with $\rho_1 \leftarrow \rho_1^*$ $\rho_2 \leftarrow \rho_2^*$:

$$-p(\rho_2^*)V + \Phi'(\rho_2^*)\mathcal{F}(\rho_1^*, \rho_2^*, V) \leqslant -p(\rho_1^*)V + \Phi'(\rho_1^*)\mathcal{F}(\rho_1^*, \rho_2^*, V).$$

Adding $\mathcal{F}(\rho_1^*, \rho_2^*, V)z^*$ on both sides of this inequality, we observe that it is sufficient to prove that

$$-p(\rho_2^*)V + \Big[\Phi'(\rho_2) + z_2\Big]\mathcal{F}(\rho_1^*, \rho_2^*, V) \leqslant -p(\rho_2^*)V + \Big[\Phi'(\rho_2^*) + z^*\Big]\mathcal{F}(\rho_1^*, \rho_2^*, V),$$

and

$$-p(\rho_1^*)V + \Big[\Phi'(\rho_1^*) + z^*\Big]\mathcal{F}(\rho_1^*, \rho_2^*, V) \leqslant -p(\rho_1^*)V + \Big[\Phi'(\rho_1) + z_1\Big]\mathcal{F}(\rho_1^*, \rho_2^*, V).$$

Since $\Phi' = \mathscr{E}$, this can be written

$$-\Big[\mathscr{E}(\rho_2^*) - \big(\mathscr{E}(\rho_2) + z_2 - z^*\big)\Big]\mathcal{F}(\rho_1^*, \rho_2^*, V) \leqslant 0, \tag{32}$$

and

$$\Big[\mathscr{E}(\rho_1^*) - \big(\mathscr{E}(\rho_1) + z_1 - z^*\big)\Big]\mathcal{F}(\rho_1^*, \rho_2^*, V) \leqslant 0. \tag{33}$$

Remarkably, these two inequalities hold. Indeed, to prove the first one, we distinguish two cases: if $\mathscr{E}(\rho_2) + z_2 - z^* \geqslant 0$, we have $\mathscr{E}(\rho_2^*) = \mathscr{E}(\rho_2) + z_2 - z^*$ and the left hand side of (32) vanishes; if $\mathscr{E}(\rho_2) + z_2 - z^* < 0$, we have $\mathscr{E}(\rho_2^*) = 0$, so that $\rho_2^* = 0$ and, consequently, $\mathcal{F}(\rho_1^*, \rho_2^*, V) = \mathcal{F}^+(\rho_1^*, V) + \mathcal{F}^-(0, V) = \mathcal{F}^+(\rho_1^*, V) \geqslant 0$. In both cases, inequality (32) holds. The same reasoning apply to (33). Thus, inequality (31) is proved and we can denote by $G(\rho_1, \rho_2, V)$ a quantity such that

$$\frac{1}{2}\Big(p(\rho_1^*) - p(\rho_2^*)\Big)V + \Big[\Phi'(\rho_2) + z_2\Big]\mathcal{F}(\rho_1^*, \rho_2^*, V) \leqslant G(\rho_1, \rho_2, V)$$

and

$$G(\rho_1, \rho_2, V) \leqslant \frac{1}{2}\Big(p(\rho_2^*) - p(\rho_1^*)\Big)V + \Big[\Phi'(\rho_1) + z_1\Big]\mathcal{F}(\rho_1^*, \rho_2^*, V).$$

We apply the first inequality to $\rho_1 \leftarrow \rho_{j-\frac12}$, $\rho_2 \leftarrow \rho_{j+\frac12}$, $z_1 \leftarrow z_{j-\frac12}$, $z_2 \leftarrow z_{j+\frac12}$ and $V \leftarrow u_j$ and the second one to $\rho_1 \leftarrow \rho_{j+\frac12}$, $\rho_2 \leftarrow \rho_{j+\frac32}$, $z_1 \leftarrow z_{j+\frac12}$, $z_2 \leftarrow z_{j+\frac32}$ and $V \leftarrow u_{j+1}$. We substract the two inequalities, and by denoting $G_j = G(\rho_{j-\frac12}, \rho_{j+\frac12}, u_j)$, we obtain

$$\begin{aligned} G_{j+1} - G_j \leqslant -\frac12\Big(p(\rho_j^\ell) - p(\rho_j^r)\Big)u_j - \frac12\Big(p(\rho_{j+1}^\ell) - p(\rho_{j+1}^r)\Big)u_{j+1} \\ + \Big[\Phi'(\rho_{j+\frac12}) + z_{j+\frac12}\Big]\Big[\mathcal{F}(\rho_{j+1}^\ell, \rho_{j+1}^r, u_{j+1}) - \mathcal{F}(\rho_j^\ell, \rho_j^r, u_j)\Big]. \end{aligned}$$

At this stage, going back to the semi-discrete mass balance equation (first equation of (26)) we observe that

$$\mathcal{F}(\rho_{j+1}^\ell, \rho_{j+1}^r, u_{j+1}) - \mathcal{F}(\rho_j^\ell, \rho_j^r, u_j) = \mathcal{F}_{j+1} - \mathcal{F}_j = -\delta x_{j+\frac12}\frac{d\rho_{j+\frac12}}{dt}(t).$$

Since $z_{j+\frac12}$ does not depend on time, we finally get

$$\begin{aligned} &\frac{\mathrm{d}}{\mathrm{d}t}\Big[\Phi(\rho_{j+\frac12}) + \rho_{j+\frac12}z_{j+\frac12}\Big] + \frac{1}{\delta x_{j+\frac12}}\Big(G_{j+1} - G_j\Big) \\ &\qquad + \frac{1}{2\delta x_{j+\frac12}}\Big[\Big(p(\rho_j^\ell) - p(\rho_j^r)\Big)u_j + \Big(p(\rho_{j+1}^\ell) - p(\rho_{j+1}^r)\Big)u_{j+1}\Big] \leqslant 0. \end{aligned} \tag{34}$$

This is the semi-discrete analog of the internal and potential energy balance law (27).

The second step consists in obtaining a semi-discrete version of the kinetic energy balance equation (28). It relies on the semi-discrete mass balance equation on the dual mesh

$$\frac{\mathrm{d}\rho_j}{\mathrm{d}t}(t) = -\frac{1}{\delta x_j}\Big(\mathscr{F}_{j+\frac12} - \mathscr{F}_{j-\frac12}\Big),$$

where $\mathscr{F}_{j+\frac12} = \mathscr{F}^+_{j+\frac12} + \mathscr{F}^-_{j+\frac12}$ with

$$\mathscr{F}^+_{j+\frac12} = \frac12\Big(\mathcal{F}^+(\rho_j^\ell, u_j) + \mathcal{F}^+(\rho_{j+1}^\ell, u_{j+1})\Big),$$

and

$$\mathscr{F}^-_{j+\frac12} = \frac12\Big(\mathcal{F}^-(\rho_j^r, u_j) + \mathcal{F}^-(\rho_{j+1}^r, u_{j+1})\Big).$$

Like for the fully discrete version, this equality can be readliy obtained from the semi-discrete mass balance equation (first equation of (26)) and the definition (9) of ρ_j. With this equation at hand, we multiply the second equation of (26) by $u_j(t)$. The left hand side gives

$$\begin{aligned} u_j\frac{\mathrm{d}(\rho_j u_j)}{\mathrm{d}t} &= \frac{\mathrm{d}}{\mathrm{d}t}\Big(\rho_j\frac{u_j^2}{2}\Big) + \frac{u_j^2}{2}\frac{\mathrm{d}\rho_j}{\mathrm{d}t} \\ &= \frac{\mathrm{d}}{\mathrm{d}t}\Big(\rho_j\frac{u_j^2}{2}\Big) - \frac{u_j^2}{2\delta x_j}\Big(\mathscr{F}_{j+\frac12} - \mathscr{F}_{j-\frac12}\Big). \end{aligned}$$

Gathering this result with the right hand side leads to

$$\begin{aligned} \frac{\mathrm{d}}{\mathrm{d}t}\Big(\rho_j\frac{u_j^2}{2}\Big) = &-\frac{1}{\delta x_j}\Big(K_{j+\frac12} - K_{j-\frac12}\Big) \\ &- \frac{1}{2\delta x_j}\Big(-\mathscr{F}^-_{j+\frac12}(u_{j+1} - u_j)^2 + \mathscr{F}^+_{j-\frac12}(u_j - u_{j-1})^2\Big) \\ &- \frac{1}{\delta x_j}u_j\Big(p(\rho_j^r) - p(\rho_j^\ell)\Big), \end{aligned}$$

with $K_{j+\frac{1}{2}} = \dfrac{u_j^2}{2}\mathscr{F}^+_{j+\frac{1}{2}} + \dfrac{u_{j+1}^2}{2}\mathscr{F}^-_{j+\frac{1}{2}}$. Since $\mathscr{F}^-_{j+\frac{1}{2}} \leqslant 0$ and $\mathscr{F}^+_{j+\frac{1}{2}} \geqslant 0$, we obtain

$$\frac{\mathrm{d}}{\mathrm{d}t}\Big(\rho_j \frac{u_j^2}{2}\Big) + \frac{1}{\delta x_j}\Big(K_{j+\frac{1}{2}} - K_{j-\frac{1}{2}}\Big) + \frac{1}{\delta x_j} u_j \Big(p(\rho_j^r) - p(\rho_j^\ell)\Big) \leqslant 0. \tag{35}$$

This is the semi-discrete analog of the kinetic energy balance equation (28).

To conclude and obtain a semi-discrete version of the entropy inequality (29), it remains to sum (34) and the mean value of (35) for j and $j+1$. Denoting

$$\eta_{j+\frac{1}{2}} = \frac{1}{2\delta x_{j+\frac{1}{2}}}\Big(\delta x_j \rho_j \frac{u_j^2}{2} + \delta x_{j+1}\rho_{j+1}\frac{u_{j+1}^2}{2}\Big) + \Phi(\rho_{j+\frac{1}{2}}) + \rho_{j+\frac{1}{2}} z_{j+\frac{1}{2}}$$

and

$$H_j = G_j + \frac{1}{2}\Big(K_{j-\frac{1}{2}} + K_{j+\frac{1}{2}}\Big),$$

we get

$$\frac{\mathrm{d}\eta_{j+\frac{1}{2}}}{\mathrm{d}t} + \frac{1}{\delta x_{j+\frac{1}{2}}}\Big(H_{j+1} - H_j\Big) \leqslant 0.$$

This is a semi-discrete version of the entropy inequality (29).

Proving the (fully discrete) entropy inequality is a fundamental issue of the analysis of numerical schemes for conservation and balance laws: it guarantees the selection of the correct weak solution, satisfying the entropy admissibility criterion. In the context of well-balanced schemes for systems with sources, the semi-discrete version of the entropy inequality is a first step in this program, see Section 4.11 of [15]. In fact, for colocalized methods based on the hydrostatic reconstruction, the fully discrete entropy inequality has been shown to hold only up to an error term vanishing as the numerical parameters tend to 0, even for discontinuous solutions [6], or by introducing *ad hoc* artificial viscosity [13]. The numerical experiments presented below do not exhibit non entropic solutions, as in can be observed with certain numerical fluxes, see Section 5 of [13].

2.3. Second order version of the WB scheme

We propose a second-order accurate version of the scheme. To this end, we make use of the principles of the MUSCL methods [63]. For the source-free problem, we refer the reader to [35] for the adaptation of this framework to the scheme described in Section 2.1. Let us denote

$$W = \mathscr{E}(\rho) + z$$

the quantity conserved by the equilibrium. The idea is to introduce a first order polynomial interpolation of the numerical unknowns in order to define new interface values. Namely, we set

$$\rho_j^- = \rho_{j-\frac{1}{2}} + \pi_{j-\frac{1}{2}}(x_j - x_{j-\frac{1}{2}}), \qquad \rho_j^+ = \rho_{j+\frac{1}{2}} + \pi_{j+\frac{1}{2}}(x_j - x_{j+\frac{1}{2}}),$$

and we proceed similarly with

$$W_j^- = W_{j-\frac{1}{2}} + \tilde{\pi}_{j-\frac{1}{2}}(x_j - x_{j-\frac{1}{2}}), \qquad W_j^+ = W_{j+\frac{1}{2}} + \tilde{\pi}_{j+\frac{1}{2}}(x_j - x_{j+\frac{1}{2}}).$$

In these formula, $\pi_{j+\frac{1}{2}}, \tilde{\pi}_{j+\frac{1}{2}}$ are some appropriately defined slopes, that accounts for a limitation mechanism in order to prevent under/overshoots in the vicinity of shocks; in such regions the scheme degrades to first order. The design of limiters is completely standard; we refer the reader to [35] and the references therein for further details. We reconstruct an interface data for the bottom topography by introducing

$$z_j^- = W_j^- - \mathscr{E}(\rho_j^-), \qquad z_j^+ = W_j^+ - \mathscr{E}(\rho_j^+).$$

Next, we set

$$z_j^{ml} = \max(z_j^-, z_j^+),$$

bearing in mind that these reconstructed quantities might vary at each time step, while the force density z does not depend on time. Finally, we reconstruct the interface densities by using the same idea as before, using the interpolated values

$$\mathscr{E}(\rho_j^{ml,r}) = \big[\mathscr{E}(\rho_j^+) + z_j^+ - z_j^{ml}\big]_+ = \big[W_j^+ - z_j^{ml}\big]_+,$$

$$\mathscr{E}(\rho_j^{ml,\ell}) = \big[\mathscr{E}(\rho_j^-) + z_j^- - z_j^{ml}\big]_+ = \big[W_j^- - z_j^{ml}\big]_+.$$

The mass fluxes are then set to

$$\mathscr{F}_j^{ml} = \mathcal{F}^+(\rho_j^{ml,\ell}, u_j) + \mathcal{F}^-(\rho_j^{ml,r}, u_j).$$

For the momentum equation, we similarly reconstruct a velocity

$$u^-_{j+\frac12} = u_j + \nu_j(x_{j+\frac12} - x_j), \qquad u^+_{j+\frac12} = u_{j+1} + \nu_{j+1}(x_{j+\frac12} - x_{j+1}),$$

where ν_j are convenient slopes defined from limiters. We then adapt accordingly the definition of the convection fluxes:

$$\begin{aligned}\mathscr{G}^{ml}_{j+\frac12} = \ & \frac{u^-_{j+\frac12}}{2}\Big(\mathcal{F}^+(\rho_j^{ml,\ell}, u_j) + \mathcal{F}^+(\rho_{j+1}^{ml,\ell}, u_{j+1})\Big) \\ & + \frac{u^+_{j+\frac12}}{2}\Big(\mathcal{F}^-(\rho_j^{ml,r}, u_j) + \mathcal{F}^-(\rho_{j+1}^{ml,r}, u_{j+1})\Big).\end{aligned}$$

The centered approximation of the pressure with

$$\Pi_{j+\frac12} = p(\rho_{j+\frac12})$$

gives a second order approximation. What is more subtle is the treatment of the source terms. So far, we have just replaced $\rho_j^{r/\ell}$ (or u_j) by the values $\rho_j^{ml,r/\ell}$ (or $u^\mp_{j\pm\frac12}$) obtained by using the limited interpolation. Proceeding similarly with the source term produces an approximation which is not consistent (essentially since the reconstructions $z_j^\pm$ used in the definition of $\rho_j^{ml,r/\ell}$ are two (second order) approximations of z at the same point x_j). A further inspection of formula (19) shows that the obstacle for having a second order approximation seems to come from the term

$$\frac{\rho_j^r - \rho_j^\ell}{2}|\delta z_j|$$

By the way, the scheme discussed in Remark 2.2 precisely disregard this term. This suggests that we should stick to the definition of the source term with (14) and just correct the first order defect; namely, we use

$$S_j^{ml} = p(\rho_j^r) - p(\rho_{j+\frac12}) - p(\rho_j^\ell) + p(\rho_{j-\frac12}) + \frac{\rho_j^r - \rho_j^\ell}{2}|\delta z_j|. \tag{36}$$

The scheme thus reads

$$\overline{\rho}_{j+\frac12} = \rho_{j+\frac12} - \frac{\delta t}{\delta x_{j+\frac12}}\Big(\mathscr{F}^{ml}_{j+1} - \mathscr{F}^{ml}_j\Big),$$

$$\overline{\rho}_j\overline{u}_j = \rho_j u_j - \frac{\delta t}{\delta x_j}\bigg(\Big(\mathscr{G}^{ml}_{j+\frac12} + \Pi_{j+\frac12}\Big) - \Big(\mathscr{G}^{ml}_{j-\frac12} + \Pi_{j-\frac12}\Big) + S_j^{ml}\bigg),$$

with $\Pi_{j+\frac12} = p(\rho_{j+\frac12})$.

Consistency. For the Shallow-Water system (when $\min(\rho_{j-\frac{1}{2}}, \rho_{j+\frac{1}{2}}) \geqslant |\delta z_j|$), (36) exactly casts as

$$(\mathbf{SW}) \qquad S_j^{ml} = \frac{\rho_{j+\frac{1}{2}} + \rho_{j+\frac{1}{2}}}{2}(z_{j+\frac{1}{2}} - z_{j-\frac{1}{2}}).$$

We recover the treatment of the pressure gradient/source term devised in Remark 2.2, which is indeed a second order approximation of $\rho\partial_x z$ at x_j. Hence, for reaching the second order accuracy, we remove from the centered well-balanced formula $p(\rho_j^r) - p(\rho_{j+\frac{1}{2}}) - p(\rho_j^\ell) + p(\rho_{j-\frac{1}{2}})$ the correction term $(\rho_j^r - \rho_j^\ell)|\delta z_j|/2$ (which produces a $O(1)$ error). This simple approach applies to more general pressure laws. We are led to evaluate the consistency error of

$$S_j^{ml} = (p(\rho_j^r) - p(\rho_{j+\frac{1}{2}})) - (p(\rho_j^\ell) - p(\rho_{j-\frac{1}{2}})) - \frac{1}{2}(\rho_j^r - \rho_j^\ell)|\delta z_j|.$$

We go back to (20), (21), (22) and (23) to obtain the following expansions

$$p(\rho_j^r) - p(\rho_{j+\frac{1}{2}}) + \frac{1}{2}\rho_j^r|\delta z_j| = \begin{cases} -p(\rho_{j+\frac{1}{2}}), & \text{if } \delta z_j \leqslant 0 \text{ and } \mathscr{E}(\rho_{j+\frac{1}{2}}) \leqslant |\delta z_j|, \\ \frac{1}{2}\delta z_j \rho_{j+\frac{1}{2}} + o(|\delta z_j|^2), & \text{if } \delta z_j \leqslant 0 \text{ and } \mathscr{E}(\rho_{j+\frac{1}{2}}) \geqslant |\delta z_j|, \\ \frac{1}{2}\delta z_j \rho_{j+\frac{1}{2}}, & \text{if } \delta z_j \geqslant 0, \end{cases}$$

$$p(\rho_j^\ell) - p(\rho_{j-\frac{1}{2}}) + \frac{1}{2}\rho_j^\ell|\delta z_j| = \begin{cases} -\frac{1}{2}\rho_{j-\frac{1}{2}}\delta z_j, & \text{if } \delta z_j \leqslant 0, \\ -\frac{1}{2}\rho_{j-\frac{1}{2}}\delta z_j + o(|\delta z_j|^2), & \text{if } \delta z_j \geqslant 0 \text{ and } \mathscr{E}(\rho_{j-\frac{1}{2}}) \geqslant |\delta z_j|, \\ -p(\rho_{j-\frac{1}{2}}), & \text{if } \delta z_j \geqslant 0 \text{ and } \mathscr{E}(\rho_{j-\frac{1}{2}}) \leqslant |\delta z_j|. \end{cases}$$

Bearing in mind that, in the case where $\mathscr{E}(\rho_{j\pm\frac{1}{2}}) \leqslant |\delta z_j|$, we have

$$p(\rho_{j\pm\frac{1}{2}}) + \delta z_j \rho_{j\pm\frac{1}{2}} = o(|\delta z_j|),$$

we obtain

$$S_j = \begin{cases} \frac{1}{2}(\rho_{j-\frac{1}{2}} + \rho_{j+\frac{1}{2}})\delta z_j + o(|\delta z_j|), & \text{if } \min\big(\mathscr{E}(\rho_{j-\frac{1}{2}}), \mathscr{E}(\rho_{j+\frac{1}{2}})\big) \leqslant |\delta z_j|, \\ \frac{1}{2}(\rho_{j-\frac{1}{2}} + \rho_{j+\frac{1}{2}})\delta z_j + o(|\delta z_j|^2), & \text{otherwise.} \end{cases}$$

The term $\frac{1}{2}(\rho_{j-\frac{1}{2}} + \rho_{j+\frac{1}{2}})\delta z_j/\delta x_j$ provides a second order accurate approximation of the source term $\rho\partial_x z$ at the point x_j. Thus, $S_j/\delta x_j$ can reach a second order accuracy away from dry/wet transition (more precisely when $\min\big(\mathscr{E}(\rho_{j-\frac{1}{2}}), \mathscr{E}(\rho_{j+\frac{1}{2}})\big) \geqslant |\delta z_j|$).

Preservation of equilibrium states. Equilibrium states (2) with no dry area (that is $W_{j+\frac{1}{2}} = \eta$) are preserved by the MUSCL reconstruction (*i.e.* $W_j^\pm = \eta$) and, as proved in the previous Section, we then obtain $\rho_j^r = \rho_j^\ell$ and $\rho_j^{ml,r} = \rho_j^{ml,\ell}$. It readily follows that the second order version of the scheme preserves equilibrium with no dry area. In the presence of dry area, the preservation of equilibrium states is also valid. However, the MUSCL reconstruction no longer exactly preserves the equilibrium states near wet/dry transitions. Nevertheless we can observe, thanks to the properties of the reconstruction that $W_j^\pm \geqslant \eta$, since at equilibrium we have $W_{j+\frac{1}{2}} = \max(\eta, z_{j+\frac{1}{2}}) \geqslant \eta$. Moreover, we have

$$W_{j+\frac{1}{2}} = \eta \Longrightarrow (W_j^+ = \eta,\ W_{j+1}^- = \eta)$$
$$W_{j+\frac{1}{2}} = z_{j+\frac{1}{2}} \Longrightarrow (\rho_j^+ = 0,\ \rho_{j+1}^- = 0).$$

Indeed, when $W_{j+\frac{1}{2}} = \eta$, we necessarily have $W_{j-\frac{1}{2}} \geqslant W_{j+\frac{1}{2}}$ and $W_{j+\frac{3}{2}} \geqslant W_{j+\frac{1}{2}}$, so that the properties of the slope-limiter implies that $\tilde{\pi}_{j+\frac{1}{2}} = 0$, ensuring the asserted property. The second line is similarly obtained since when $W_{j+\frac{1}{2}} = z_{j+\frac{1}{2}}$, we have $\rho_{j+\frac{1}{2}} = 0 \leqslant \min(\rho_{j-\frac{1}{2}}, \rho_{j+\frac{3}{2}})$ so that $\pi_{j+\frac{1}{2}} = 0$. With these properties at hand, it is now straightforward to prove that $\rho_j^{ml,r} = \rho_j^{ml,\ell}$. Indeed, we distinguish four cases. First, if $W_{j-\frac{1}{2}} = \eta$ and $W_{j+\frac{1}{2}} = \eta$ then we have $W_j^{\pm} = \eta$ which leads to the equality $\rho_j^{ml,r} = \rho_j^{ml,\ell}$. If $W_{j-\frac{1}{2}} = z_{j-\frac{1}{2}}$ and $W_{j+\frac{1}{2}} = z_{j+\frac{1}{2}}$ then $\rho_j^{\pm}$ vanish, so that $z_j^{\pm} = W_j^{\pm}$ and the equality $\rho_j^{ml,r} = \rho_j^{ml,\ell}$ still holds. Finally the two last cases are symmetric. For instance, if $W_{j-\frac{1}{2}} = z_{j-\frac{1}{2}}$ and $W_{j+\frac{1}{2}} = \eta$ then we have $\rho_j^- = 0$ and $W_j^+ = \eta$. This implies that $\eta \leqslant W_j^- = z_j^- \leqslant z_j^{ml}$. Thus, $\rho_j^{ml,r}$ and $\rho_j^{ml,\ell}$ both vanish in this case. The equality $\rho_j^{ml,r} = \rho_j^{ml,\ell}$ is ensured in the four possible cases and, as previously, it guarantees that the second order version of the scheme preserves the equilibrium states (2).

3. Numerical experiments

To illustrate the ability of the proposed approach in handling balance laws with complex source terms, we challenge the scheme against several benchmark tests, in 1D and 2D. When it is possible, to facilitate quantitative comparisons with existing numerical results, precise references to equivalent figures in the literature have been included, enabling direct comparisons. For each proposed comparison, the physical parameters are identical while slight variations in numerical parameters may occur (depending on the reference). However, despite of these potential differences in numerical settings, fair comparisons can be readily conducted.

The presented simulations are performed for the system written in the form

$$\begin{aligned} &\partial_t \rho + \partial_x(\rho u) = 0, \\ &\partial_t(\rho u) + \partial_x(\rho u^2 + g\rho^\gamma/\gamma) = -g\rho\partial_x z \end{aligned} \tag{37}$$

with $g > 0$, the gravity constant and with a γ-law for the pressure $p(\rho) = \rho^\gamma/\gamma$, but it also applies for general pressure laws. For the sake of comparison, we treat different test cases from the literature for the Shallow-Water equation ($\gamma = 2$). We also check that equilibrium solutions are preserved for different values of γ (1.4, 2, 3, 4) and provide simulations near equilibrium for $\gamma = 1.4$ and 3.

For all the 1D simulations, the time step is fixed at each time iteration by imposing the following equality

$$\delta t = C_{\delta t} \; \frac{\delta x}{\max_j |u_j| + \max_j c(\rho_{j+1/2})}$$

where $C_{\delta t}$ is a constant whose value is made precise in the description of each test case.

3.1. Preservation of equilibrium solutions

We first check that the order 1 and order 2 schemes solve exactly the equilibrium solutions for $\gamma \in \{1.4, 2, 3, 4\}$. The computational domain is $[0, 20]$. We choose a bottom topography with a parabolic obstacle defined by

$$z(x) = \begin{cases} 0.2 - 0.05(x-10)^2, & \text{if } \; 8 < x < 12, \\ 0, & \text{otherwise.} \end{cases}$$

Lake at rest without dry area. A stationary solution of the problem is given by

$$\rho_{\text{eq}}(x) = (\gamma - 1)\Big(0.3 - z(x)\Big)^{\dfrac{1}{\gamma - 1}} \quad \text{and} \quad u_{\text{eq}}(x) = 0.$$

It satisfies

$$\mathcal{E}(\rho_{\text{eq}}) + z = 0.3.$$

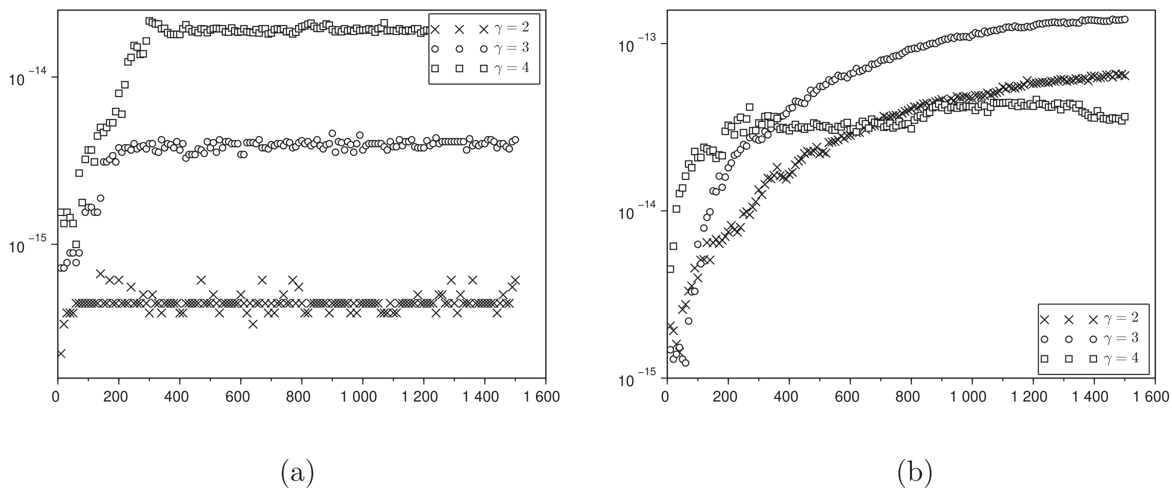

FIGURE 3. Preservation of equilibrium solutions without a dry area: L^∞-norm of the difference between the numerical solution and the equilibrium solution (initial data) as a function of the time. (a) Height:$\|\rho - \rho_{\text{eq}}\|_\infty$. (b) Velocity $\|u\|_\infty$.

We first use this equilibrium solution as an initial data. The final time of the simulation is set to $T = 1500$ and $C_{\delta t} = 0.5$. The schemes (first and second order) preserve the equilibrium solution up to the machine precision whatever is the mesh size ($\delta x = 1,\ 0.1,\ 0.01$). To illustrate this behaviour, we present in Figure 3 the L^∞-norm of the difference between the first order numerical solution and the equilibrium as a function of time for $\delta x = 0.01$ and $\gamma = 2$, 3 or 4. The errors are even smaller for $\gamma = 1.4$ and for $\delta x = 1$ or 0.1. The same results are obtained for the second order version of the scheme.

Next, for $\gamma = 2$, we initialize the computation by a constant density $\rho_{j+\frac{1}{2}} = \sum_k \delta x_{k+\frac{1}{2}} \rho_{\text{eq}}(x_{k+\frac{1}{2}})$ and $u_j = 0$. We perform the simulation with $C_{\delta t} = 0.5$ up to $T = 10000$. In Figure 4, we present the time evolution of the L^1-norm $\|\rho - \rho_{\text{eq}}\|$ of the difference between the numerical solution and the equilibrium for several mesh sizes ($\delta x = 0.1,\ 0.2,\ 0.4$ for the first order scheme and $\delta x = 0.4$ for the second order scheme). We observe that the numerical solution goes to equilibrium in long time. The error decreases to machine precision and this happens even more rapidly as the mesh becomes coarser. This is probably due to the fact that the use of a coarser mesh induces a larger numerical diffusion.

Lake at rest with a dry area. Another stationary solution of the problem is given by a vanishing velocity and

$$\rho_{\text{eq}}(x) = \begin{cases} (\gamma-1)\Big(0.1 - z(x)\Big)^{\dfrac{1}{\gamma-1}}, & \text{if } \ x < 10-\sqrt{2} \text{ or } x > 10+\sqrt{2}, \\ 0, & \text{otherwise}, \end{cases}$$

so that there is a dry zone at the top of the obstacle for x between $10-\sqrt{2}$ and $10+\sqrt{2}$. It satisfies

$$\mathcal{E}(\rho_{\text{eq}}) + z = \max(0.1, z).$$

As previously, we first set the initial data as the equilibrium solution. The final time of the simulation is set to $T = 1000$ and $C_{\delta t}$ is set to 0.5. We observe that the schemes (first and second order versions) exactly preserve the initial state whatever is the mesh size ($\delta x = 1,\ 0.1,\ 0.01$). We present in Figure 5 the L^∞-norm of the difference between the first order numerical solution and the equilibrium as a function of time for $\delta x = 0.01$ and $\gamma = 2$, 3 or 4. The errors are even smaller for $\gamma = 1.4$ and for $\delta x = 1$ or 0.1. The same results are obtained for the second order version of the scheme.

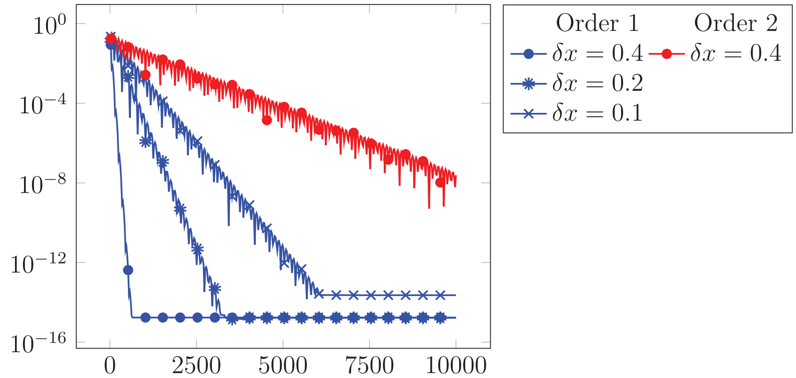

FIGURE 4. Convergence towards equilibrium solutions without dry area: Time evolution of the L^1-norm $\|\rho - \rho_{eq}\|_{L^1}$ of the difference between the numerical solution and the equilibrium solution.

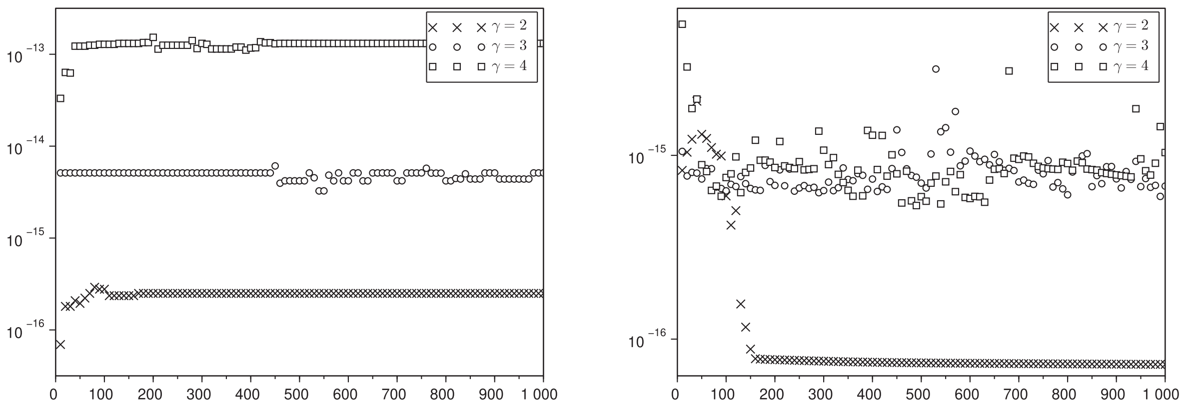

(a) (b)

FIGURE 5. Preservation of equilibrium solutions with a dry area: L^∞-norm of the difference between the numerical solution and the equilibrium solution (initial data) as a function of the time. (a) Height:$\|\rho - \rho_{\rm eq}\|_\infty$. (b) Velocity $\|u\|_\infty$.

Next, for $\gamma = 2$, as in the case without dry area, we initialize the computation by a constant density $\rho_{j+\frac{1}{2}} = \sum_k \delta x_{k+\frac{1}{2}} \rho_{\rm eq}(x_{k+\frac{1}{2}})$ and $u_j = 0$. We perform the simulation with $C_{\delta t} = 0.5$ up to $T = 10000$. In Figure 6, we present the time evolution of the L^1-norm $\|\rho - \rho_{\rm eq}\|$ of the difference between the numerical solution and the equilibrium for several mesh sizes ($\delta x = 0.025$, 0.05, 0.1 for the first order scheme. We observe that the numerical solution goes to equilibrium but in very long time. In a first phase, the error decreases exponentially fast and, as in the case without dry area, the decay slows down with a finer mesh. In a second phase, the error decreases further, but much slowlier. That is likely attributed to the handling of dry area.

3.2. Perturbations of the lake at rest solution

Referring to [53] (see also [5, 19]), we investigate the propagation of small perturbations of the lake at rest steady solution. As in the literature we provide the results for $\gamma = 2$ but we also perform the simulations for

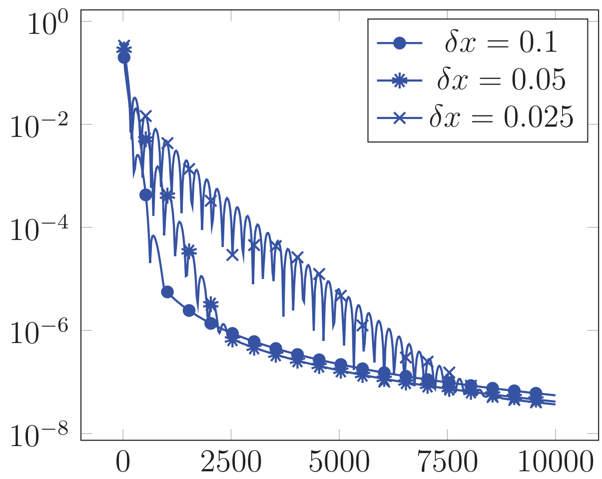

FIGURE 6. Convergence towards equilibrium solutions with dry area: Time evolution of the L^1-norm $\|\rho - \rho_{eq}\|_{L^1}$ of the difference between the numerical solution and the equilibrium solution.

$\gamma = 1.4$ and $\gamma = 3$. The computational domain is the interval $[0, 2]$ and the gravity constant is $g = 9.8$. The bottom topography is defined by

$$z(x) = \begin{cases} -1 + 0.25\Big(1 + \cos\big(10\pi(x - 0.5)\big)\Big), & \text{if } 1.4 < x < 1.6, \\ -1, & \text{otherwise.} \end{cases}$$

The initial data are given by

$$u(x) = 0, \quad \forall x \in [0, 2],$$

and

$$\rho(x) = \begin{cases} \Big(-(\gamma - 1)z(x)\Big)^{\dfrac{1}{\gamma - 1}} + 0.001, & \text{if } 1.1 < x < 1.2, \\ \Big(-(\gamma - 1)z(x)\Big)^{\dfrac{1}{\gamma - 1}}, & \text{otherwise.} \end{cases}$$

This is a steady state solution perturbed by a pulse of amplitude 10^{-3}. Two opposite waves appear, and the right wave goes over the bump. The final time of the simulation is set respectively to $T = 0.2$ for $\gamma = 2$, $T = 0.15$ for $\gamma = 1.4$ and $T = 0.25$ for $\gamma = 3$. The time step is fixed by chosing $C_{\delta t} = 0.5$. The numerical results are presented in Figure 7 for $\gamma = 2$, Figure 8 for $\gamma = 1.4$ and Figure 9 for $\gamma = 3$ (the "free surface" $\mathscr{E}(\rho) + z$ at left and the discharge $q = \rho u$ at right). A reference solution is computed with $\delta x = 4 \times 10^{-4}$, it is plotted in black solid line. The numerical results obtained with $\delta x = 10^{-2}$ are plotted in blue dashed line for the first order scheme and in red dotted line for the second order scheme. We clearly see the advantage of running the second order scheme. The results are comparable to those obtained in the literature for $\gamma = 2$. Figure 7 can be indeed directly compared to Figure 13 of [19] or Figure 3.1 of [5]. We observe that a perturbation forms and returns backward when the right wave passes over the bump. The smaller γ (close to 1), the greater the amplitude of the perturbation. This perturbation almost vanishes for $\gamma = 3$.

3.3. Flow over an isolated bump

In this Section, we consider flows governed by Shallow-Water equations ($\gamma = 2$), over an isolated convex obstacle which is assumed to be symmetric with respect to its crest. The flow goes from the left to the right.

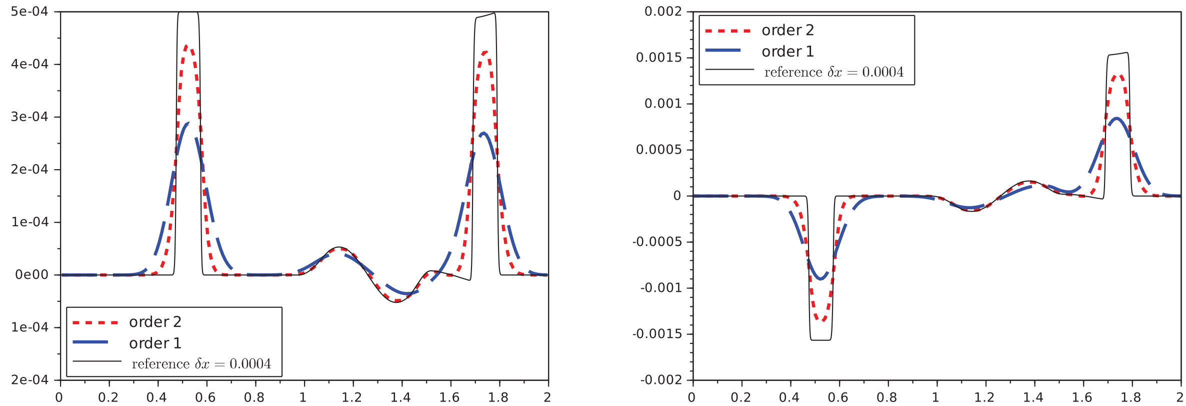

(a) (b)

FIGURE 7. Perturbations of the lake at rest ($\gamma = 2$): numerical solutions obtained for $\delta x = 0.01$. (a) Free surface $\rho + z$. (b) Discharge ρu.

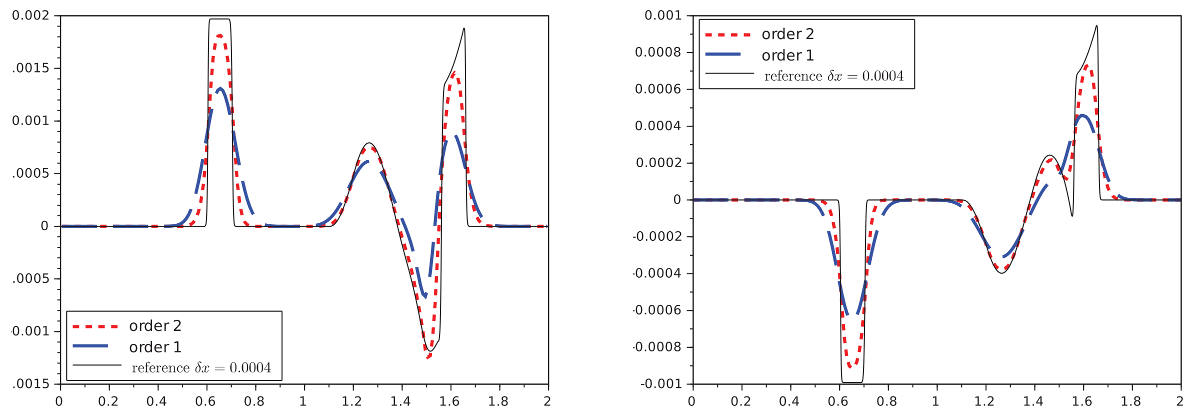

(a) (b)

FIGURE 8. Perturbations of the lake at rest ($\gamma = 1.4$): numerical solutions obtained for $\delta x = 0.01$. (a) Free surface $(\rho) + z$. (b) Discharge ρu.

Its velocity and height far from the obstacle are denoted by $u_0 > 0$ and ρ_0. A transient motion develops at the obstacle and moves in both directions. After sufficient time has elapsed, the flow reaches a steady state in the vicinity of the obstacle; transient structures move away from the obstacle and reach asymptotic states. The asymptotic states can be entirely characterized from the values of u_0 and ρ_0 and the geometry of the bump, as it is fully detailed in [48]. For the sake of completeness, we recall here the different situations which can occur and how the asymptotic reference solution can be computed in the different cases. Let us denote by F_0 be the Froude number computed from u_0 and ρ_0:

$$F_0 = \frac{u_0}{\sqrt{g\rho_0}},$$

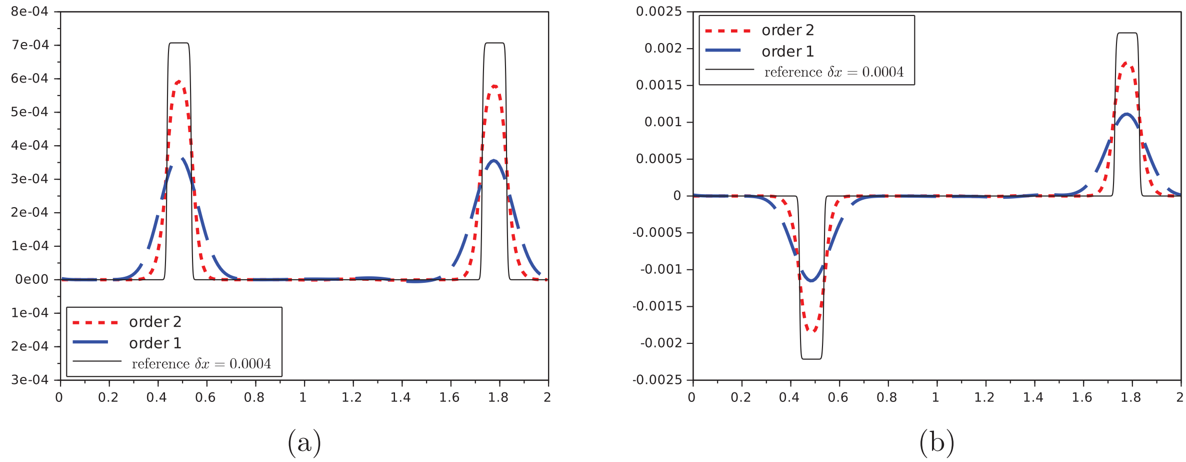

FIGURE 9. Perturbations of the lake at rest ($\gamma = 3$): numerical solutions obtained for $\delta x = 0.01$. (a) Free surface $(\rho) + z$. (b) Discharge ρu.

while Z_c stands for the height of the obstacle crest. We distinguish two situations depending on the values of the coefficient

$$M_0 = \frac{1}{2}F_0^2 - \frac{3}{2}F_0^{2/3} + 1$$

compared to the normalized height of the obstacle crest

$$M_c = \frac{Z_c}{\rho_0}.$$

In the case where

$$M_c < M_0,$$

the flow reaches a steady state. More precisely, when $F_0 < 1$ the free surface at the steady state dips symmetrically over the symmetrical obstacle (see Fig. 10a) whereas when $F_0 > 1$ the steady state rises over the obstacle (see Fig. 10b). The reference solution can be obtained by solving the steady state equations

$$\begin{cases} \dfrac{u^2}{2g} + \rho + z = \text{constant}_1, \\ \rho u = \text{constant}_2. \end{cases}$$

Using the background state (ρ_0, u_0) far from the obstacle, we can thus obtain ρ from

$$\frac{\rho_0^2 u_0^2}{2g\rho^2} + \rho + z = \frac{u_0^2}{2g} + \rho_0,$$

and then $u = \rho_0 u_0/\rho$. Note that ρ and u depends on the space variable x since in these equations z is a function of x.

The situation is more intricate when

$$M_c > M_0.$$

The obstacle partially blocks the flow, a bore forms around the obstacle and the flow becomes discontinuous, hydraulic jumps appear. A discontinuity appears downstream the obstacle and propagates towards the left. The flow is sonic at the crest of the obstacle, that is, denoting (ρ_c, u_c) the flow state at the crest of the obstacle, we have $u_c = \sqrt{g\rho_c}$. Upstream the obstacle, two slightly different situations can asymptotically occur. In the first case, a discontinuity appears after the obstacle and propagates towards the right (see Fig. 10c) whereas in the second case, a stationary shock lies above the obstacle (see Fig. 10d). In both cases, a rarefaction wave allows the flow to go back to the background state $(\rho_0,\, u_0)$. The asymptotic reference solution can be obtained as follows. We denote by (ρ_A, u_A) the constant state reached after the downstream hydraulic jump (before the obstacle). It is linked to the background state (ρ_0, u_0) by the following Rankine-Hugoniot condition

$$\rho_A u_A = \rho_A u_0 + (\rho_0 - \rho_A)\sqrt{\frac{g}{2}\frac{\rho_A}{\rho_0}(\rho_0 + \rho_A)}.$$

Moreover, it is also linked to the state above the obstacle by steady state equations

$$\begin{cases} \dfrac{u_A^2}{2g} + \rho_A = \dfrac{u_c^2}{2g} + \rho_c + Z_c, \\ \rho_A u_A = \rho_c u_c. \end{cases}$$

Thus, since $\rho_c u_c = \sqrt{g}\rho_c^{3/2}$, ρ_A can be obtained by solving

$$\rho_c^3 + 2\rho_A^3 = (3\rho_c + 2Z_c)\rho_A^2,$$

where

$$\rho_c = \left(\rho_A \frac{u_0}{\sqrt{g}} + (\rho_0 - \rho_A)\sqrt{\frac{1}{2}\frac{\rho_A}{\rho_0}(\rho_0 + \rho_A)}\right)^{\frac{2}{3}}.$$

Next, we compute the asymptotic reference solution after the bore. We first assume that we are in the situtation where an hydraulic jump propagates away from the obstacle. We are led to compute two constant states to compute (ρ_B, u_B) and (ρ_x, u_x) (see Fig. 10c). The states (ρ_c, u_c) and (ρ_B, u_B) are linked by steady states equations

$$\rho_c^3 + 2\rho_B^3 = (3\rho_c + 2Z_c)\rho_B^2, \quad (\rho_B \neq \rho_A).$$

It allows us to compute ρ_B since now ρ_c is known. Then $u_B = \rho_c u_c/\rho_B$. Next, the states (ρ_B, u_B) and (ρ_x, u_x) are linked by the Rankine-Hugoniot condition

$$\rho_B u_B = \rho_B u_x + (\rho_x - \rho_B)\sqrt{\frac{g}{2}\frac{\rho_B}{\rho_x}(\rho_x + \rho_B)}$$

Finally, the states (ρ_x, u_x) and (ρ_0, u_0) are linked by a rarefaction wave so that the Riemann invariants are preserved

$$u_x - 2\sqrt{g\rho_x} = u_0 - 2\sqrt{g\rho_0}.$$

Thus, ρ_x can be obtained by solving

$$\rho_B u_B = \rho_B\Big(u_0 - 2\sqrt{g\rho_0} + 2\sqrt{g\rho_x}\Big) + (\rho_x - \rho_B)\sqrt{\frac{g}{2}\frac{\rho_B}{\rho_x}(\rho_x + \rho_B)}.$$

The displacement velocity of the shock is $(\rho_x u_x - \rho_B u_B)/(\rho_x - \rho_B)$. We distinguish now two cases: if this velocity is positive the shock propagates away from the obstacle and we have obtained the asymptotic reference solution (see Fig. 10c); if this velocity is negative, the obtained solution is not physically relevant and should be disregarded. We have to construct a solution with a stationary shock above the obstacle. In this case, we are left with the task of determining three states (ρ_-, u_-), (ρ_+, u_+) and ρ_x, u_x (see Fig. 10d). The states (ρ_A, u_A) and (ρ_-, u_-) are linked by steady state equations

$$\begin{cases} \dfrac{u_-^2}{2g} + \rho_- + Z_* = \dfrac{u_A^2}{2g} + \rho_A, \\ \rho_- u_- = \rho_A u_A, \end{cases}$$

where Z_* stands for the height of the obstacle at the shock position. The states (ρ_-, u_-) and (ρ_+, u_+) are linked by the Rankine-Hugoniot conditions for a stationary shock

$$\begin{cases} \rho_- u_- = \rho_+ u_+, \\ \rho_+ u_+ - \sqrt{\dfrac{g}{2}\rho_+\rho_-(\rho_- + \rho_+)} = 0. \end{cases}$$

The states (ρ_+, u_+) and (ρ_x, u_x) are linked by steady state equations

$$\begin{cases} \dfrac{u_+^2}{2g} + \rho_+ + Z_* = \dfrac{u_x^2}{2g} + \rho_x, \\ \rho_+ u_+ = \rho_x u_x. \end{cases}$$

Finally, as before, the states (ρ_x, u_x) and (ρ_0, u_0) are linked by a rarefaction wave

$$u_x - 2\sqrt{g\rho_x} = u_0 - 2\sqrt{g\rho_0}.$$

Thus, we deal with the four following equations

$$\begin{cases} \dfrac{\rho_A^2 u_A^2}{2g\rho_-^2} + \rho_- + Z_* = \dfrac{u_A^2}{2g} + \rho_A, \\ \rho_A u_A - \sqrt{\dfrac{g}{2}\rho_+\rho_-(\rho_- + \rho_+)} = 0 \\ \dfrac{\rho_A^2 u_A^2}{2g\rho_+^2} + \rho_+ + Z_* = \dfrac{\rho_A^2 u_A^2}{2g\rho_x^2} + \rho_x, \\ \dfrac{\rho_A u_A}{\rho_x} - 2\sqrt{g\rho_x} = u_0 - 2\sqrt{g\rho_0}, \end{cases}$$

to determine ρ_-, ρ_+, ρ_x and Z_*.

In conclusion, there exists four different classes of asymptotic solutions as illustrated in Figure 10. We numerically investigate these cases in Sections 3.3.1 to 3.3.3. The obstacle is defined by

$$z(x) = \frac{1}{10}\left(1 - \frac{x^2}{16}\right),$$

so that $Z_c = 0.1$. We fix $\rho_0 = 0.2$ and compute the velocity u_0 from different values of $F_0 = 0.2, 0.3, 0.7, 1.9$, the gravity g being fixed to 9.8. In these test cases, we set $C_{\delta t} = 0.5$.

Finally, to allow quantitive comparisons with the literature, we present in Section 3.3.4 two test cases from [19]. They correspond to situtations described in Sections 3.3.1 and 3.3.3, but we take exactly the same physical and numerical parameters as in [19].

Note that the steady states obtained in all these cases in the vicinity of the obstacle are not preserved by the first order and the second order versions of the scheme (since the velocity does not vanish). This leads to a discretization error proportional to the mesh size at the equilibrium. This error becomes particularly noticeable on the approximation of the discharge ρu which should be constant at equilibrium. Hence having established the accuracy of the schemes for handling equilibrium at rest (see Sects. 3.1 and 3.2), these test cases are interesting to check whether they exhibit degraded performance near other equilibria.

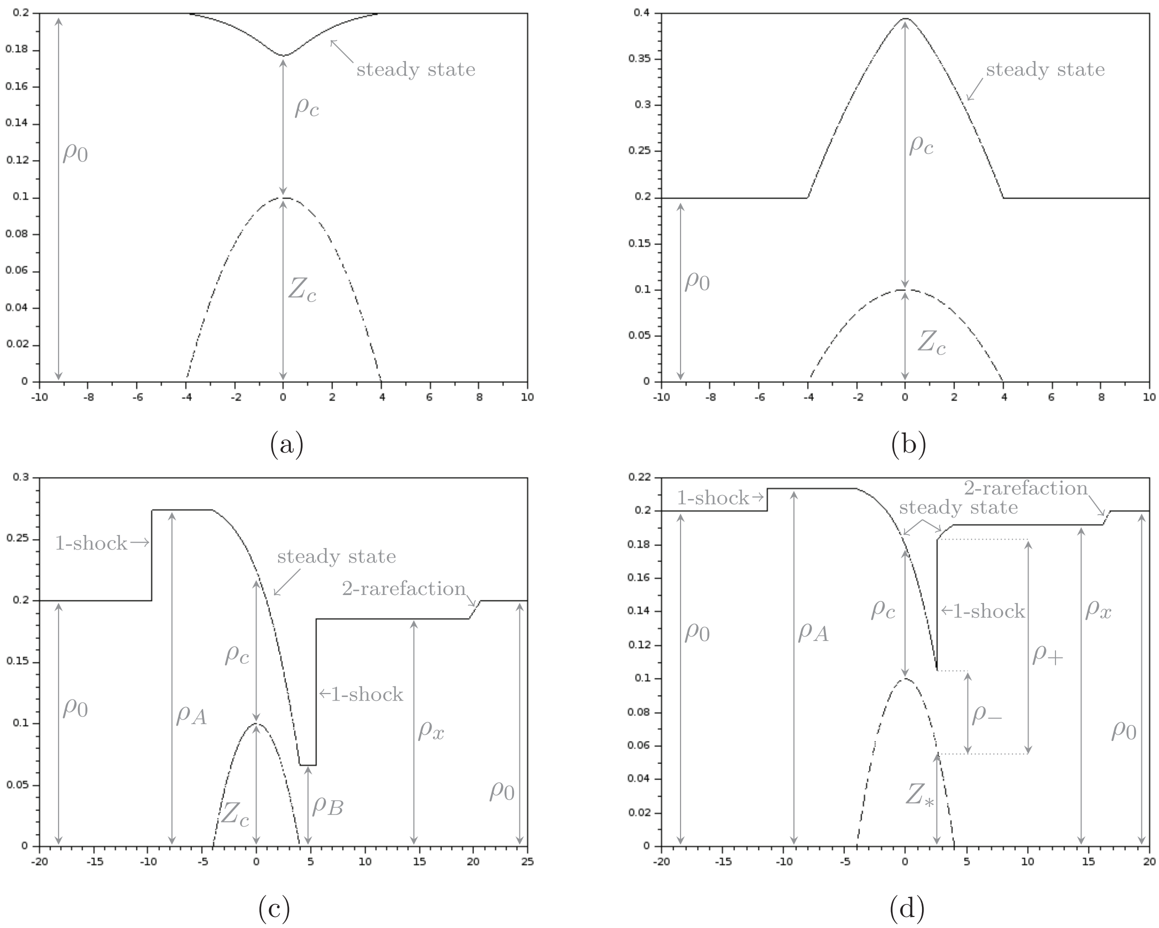

FIGURE 10. Flow over an isolated obstacle: structure of the asymptotic solution. Free surface (solid lines) and obstacle (dotted lines). (a) $M_c < M_0$ and $F_0 > 1$. (b) (b) $M_c < M_0$ and $F_0 > 1$. (c) $M_c > M_0$, upstream moving shock. (d) $M_c > M_0$, stationary shock.

3.3.1. Cases $F_0 = 0.2$ and $F_0 = 1.9$

In these two cases, we have $M_c < M_0$. As expected, the numerical solutions reach a steady state. The results obtained at time $T = 2000$ with our schemes (order 1 and order 2) are presented in Figures 11 and 12 for $\delta x = 0.05$. We obtain a good agreement with the reference profile computed with the procedure explained above. In the case $F_0 = 0.2$, the free surface dips over the obstacle whereas in the case $F_0 = 1.9$, it rises over the bump.

In Figure 13, we present the discrete error in L^1-norm as a function of the mesh size. As expected, we observe that the MUSCL reconstruction procedure allows to reach the second order accuracy for the velocity u and the height h.

3.3.2. Case $F_0 = 0.3$

In this case, we have $M_c > M_0$, this is the situation illustrated in Figure 10d. A stationary shock appears behind the obstacle. The result obtained at time $T = 30$ with our scheme (order 1 and order 2) are presented in Figure 14 for $\delta x = 0.1$. We also represent with a solid line the asymptotic reference profile. We observe

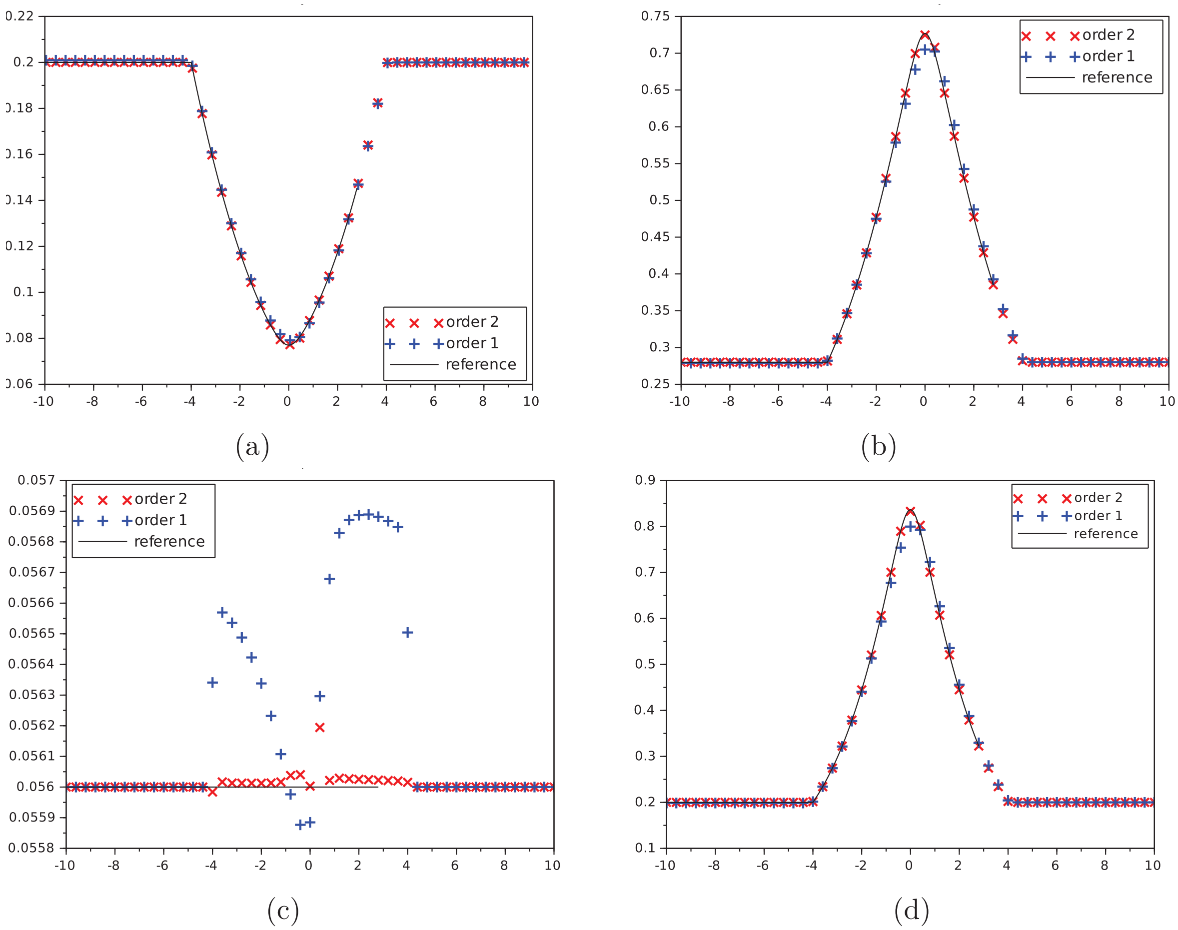

FIGURE 11. Flow over an isolated obstacle: numerical solutions obtained for $F_0 = 0.2$, $\delta x = 0.05$ at $T = 2000$. (a) Height ρ. (b) Velocity u. (c) Discharge ρu. (d) Froude number.

that the constant states ρ_A and ρ_+, the value ρ_- and the equilibrium profiles (before and after the stationary shock) perfectly match with the reference profile. However, the numerical solutions at time $T = 30$ present some additional structures compared to the reference asymptotic solution. These additional structures appear near the upstream shock and near the downstream rarefaction wave. Since the obtained numerical solutions seems to be converged with respect to δx and δt, we guess that we face transient structures that do not appear, by definition, in the asymptotic profile. We plot in Figures 15 and 16 a zoom on the structure for three larger final times $T = 100$, $T = 250$ and $T = 2000$. We indeed observe that the bump in Figure 15 and the oscillations in Figure 16 vanish as the time increases.

3.3.3. *Case* $F_0 = 0.7$

In this case, we still have $M_c > M_0$, but now in the situation of Figure 10c. The shock which appears behind the obstacle is moving to the right. The results obtained at time $T = 30$ with our schemes (order 1 and order 2) are presented in Figure 17 for $\delta x = 0.1$. We also represent with a solid line the asymptotic reference profile. Again, we observe that the constant states ρ_A, ρ_B, ρ_x and the equilibrium profile perfectly match with the reference profile. The position of the shocks is also in agreement with the reference asymptotic solution.

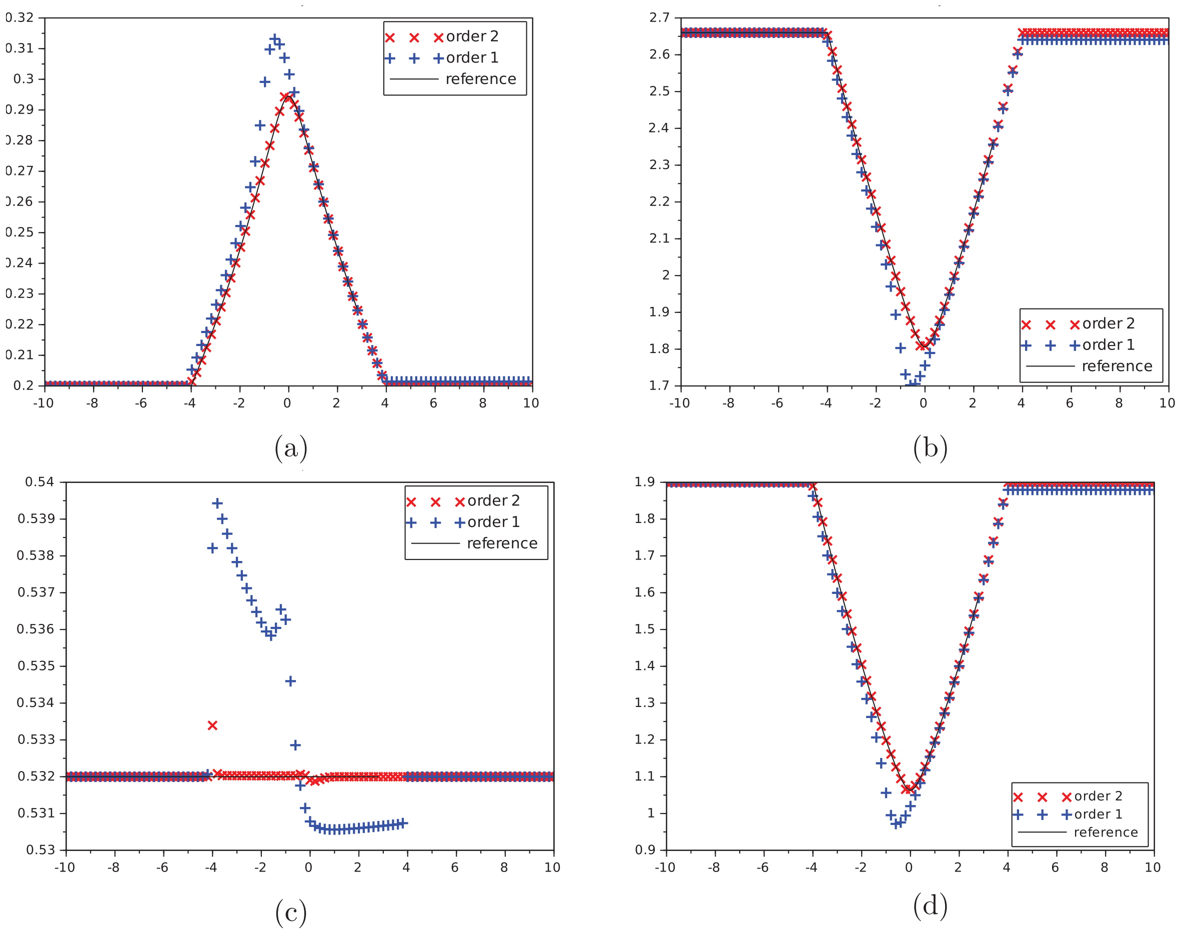

FIGURE 12. Flow over an isolated obstacle: numerical solutions obtained for $F_0 = 1.9$, $\delta x = 0.04$ at $T = 2000$. (a) Height ρ. (b) Velocity u. (c) Discharge ρu. (d) Froude number.

As previously, at time $T = 30$, we also observe an additional transient structure in the numerical solutions compared to the reference asymptotic solution in the neighborhood of the rarefaction wave.

3.3.4. Cases from the literature

The test cases presented in the three previous subsections illustrate every potential situations for a flow over a bump. However, they do not allow for quantitative comparisons with the results from the literature. To make such comparisons possible, we provide in this section two tests cases taken from [19] using exactly the same physical and numerical parameters. The flows are governed by Shallow-Water equations ($\gamma = 2$). The gravity is set to $g = 9.8$ and $C_{\delta t} = 0.5$.

The first test is the Test 1 presented in Section 5.3 of [19]. It corresponds to the situation illustrated in Section 3.3.1 (see Fig. 12). The computational domain is $[0, 10]$ and the final time $t = 100$. The bottom topography is given by

$$z(x) = -1 + 0.3 \exp\big(-(x-5)^2\big).$$

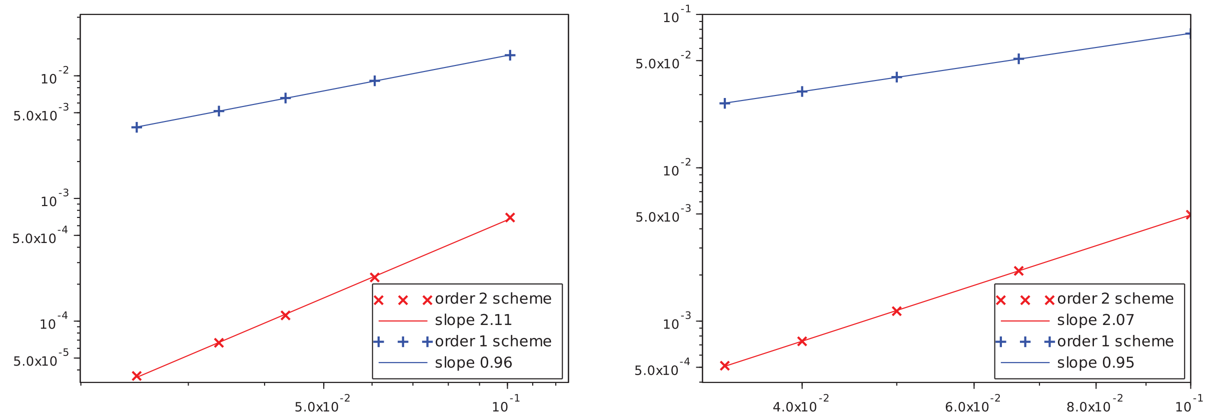

(a) (b)

FIGURE 13. Flow over an isolated obstacle: discrete error in L^1-norm as a function of the mesh size. (a) Height ρ. (b) Velocity u.

We consider the equilibrium solution given by

$$\rho u = 2 \quad \text{and} \quad \rho + z + \frac{u^2}{2g} = 2.$$

The numerical results we obtained are presented in Figure 18. As in Figure 12, we obtain a free surface rising over the bump and the discharge ρu presents some oscillations whereas it should be constant. The Figure 18 can be directly compared to Figure 2 of [19] and the results are similar. The oscillations on the discharge ρu are of order δx (or δx^2 for the second order scheme). For this test case, we also provide in Figure 19 the time evolution of the L^1-norm $\|\rho - \rho_{eq}\|_{L^1}$ of the difference between the numerical solution and the equilibrium solution for different mesh sizes (for the first and second order versions of the scheme). It does not reach the machine precision since the equilibrium is not preserved by the scheme in this case. Instead, we observe a residual error due to space discretisation. It confirms the first or second order convergence of the scheme.

The second test case is the Test 2 proposed in Section 5.4 of [19]. The computation is performed on the interval $[0, 25]$ and the final time is $t = 200$. The bottom topography is given by

$$z(x) = \begin{cases} 0.2 - 0.05(x-10)^2, & \text{if } 8 < x < 12, \\ 0, & \text{otherwise.} \end{cases}$$

With $q = \rho u$, the boundary conditions are given by

$$q(0,t) = 0.18 \quad \text{and} \quad \rho(25,t) = 0.33, \quad \forall t \geqslant 0.$$

The steady state includes a smooth transition and a stationary shock. It corresponds to the situation illustrated in Section 3.3.2 (see Fig. 14). The numerical results we obtained are presented in Figure 20. These results can be directly compared to Figure 3 of [19] (see also [5], Fig. 3.8, Sect. 3.2.3, [23], Fig. 2.23 to 2.27, Sect. 2.2.2.2 or [55], Figs. 11 and 12). We obtain similar results (a small oscillation on the discharge ρu in the smooth transition and an overshoot in the shock). We also provide in Figure 21 the time evolution of the L^1-norm $\|\rho - \rho_{eq}\|_{L^1}$ of the difference between the numerical solution and the equilibrium solution for different mesh sizes (for the first and second order versions of the scheme). As previously, it does not reach the machine precision since the equilibrium is not preserved by the scheme in this case. Instead, we observe a residual error due to space

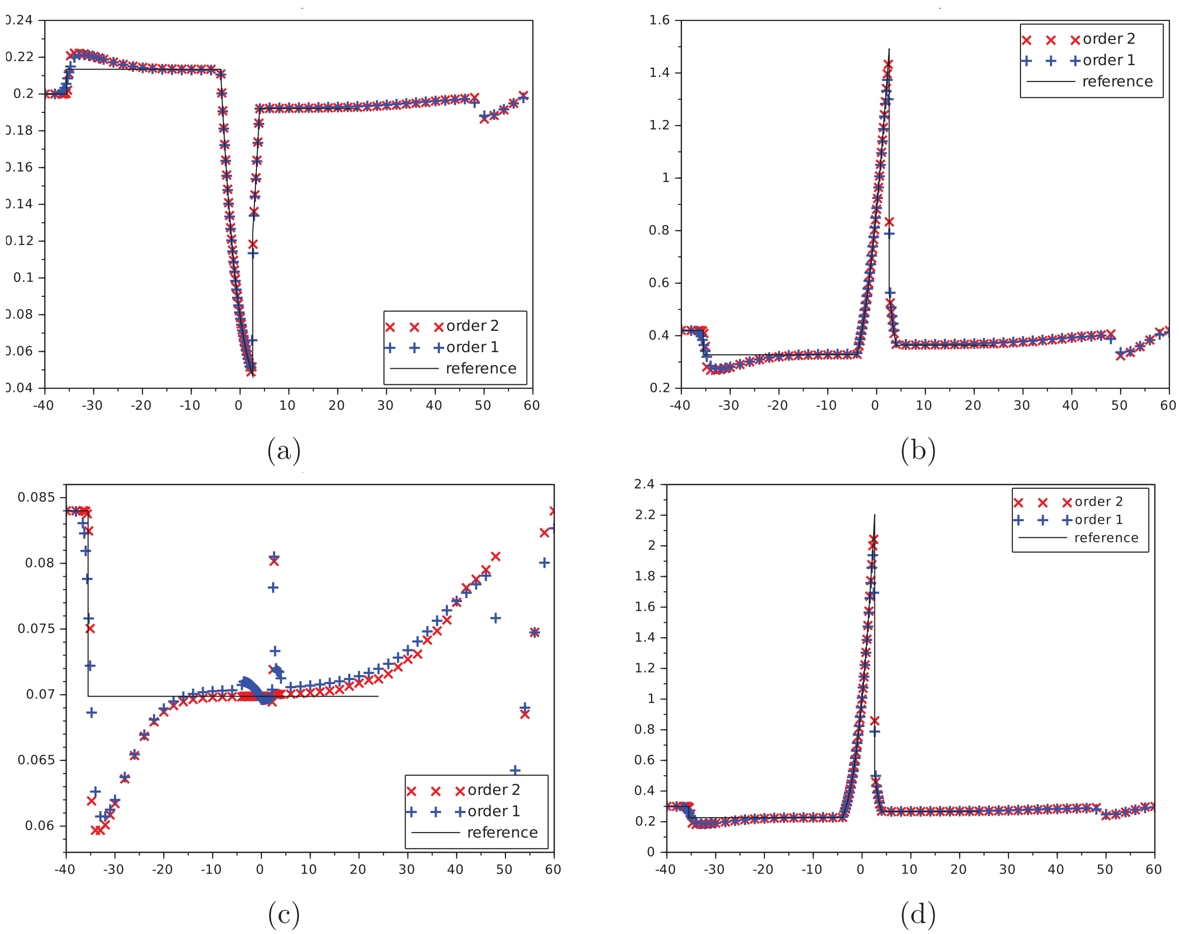

FIGURE 14. Flow over an isolated obstacle: numerical solutions obtained for $F_0 = 0.3$, $\delta x = 0.1$ at $T = 30$. (a) Height ρ. (b) Velocity u. (c) Discharge ρu. (d) Froude number.

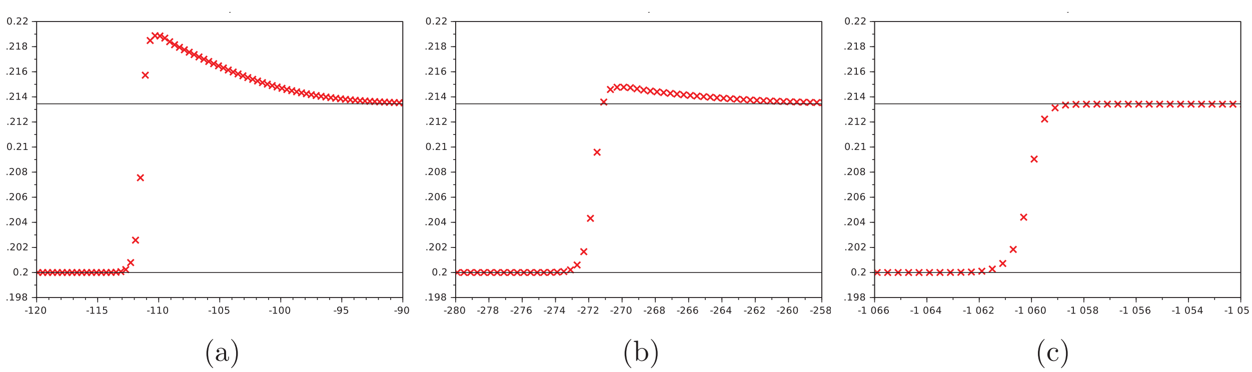

FIGURE 15. Flow over an isolated obstacle: numerical solutions obtained for $F_0 = 0.3$, $\delta x = 0.2$, zoom on the density. (a) $T = 100$. (b) $T = 250$. (c) $T = 1000$.

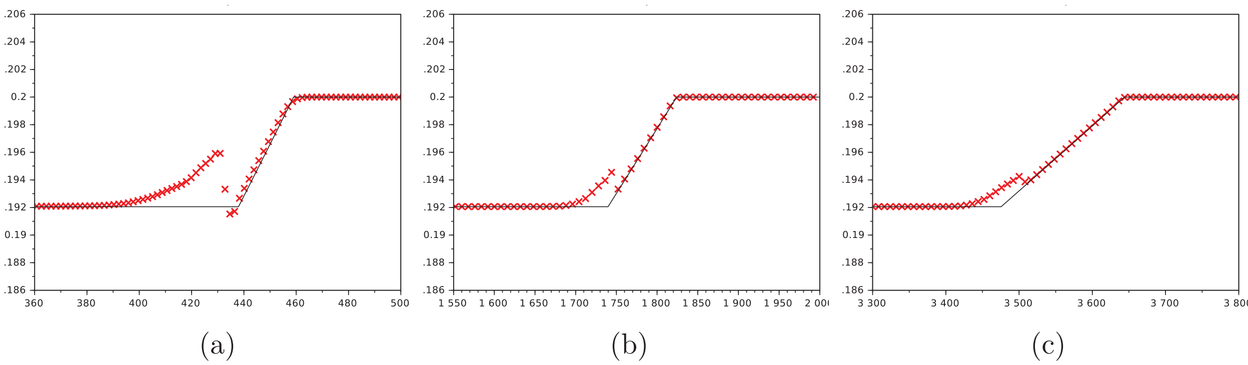

FIGURE 16. Flow over an isolated obstacle: numerical solutions obtained for $F_0 = 0.3$, $\delta x = 0.2$, zoom on the density. (a) $T = 250$. (b) $T = 1000$. (c) $T = 2000$.

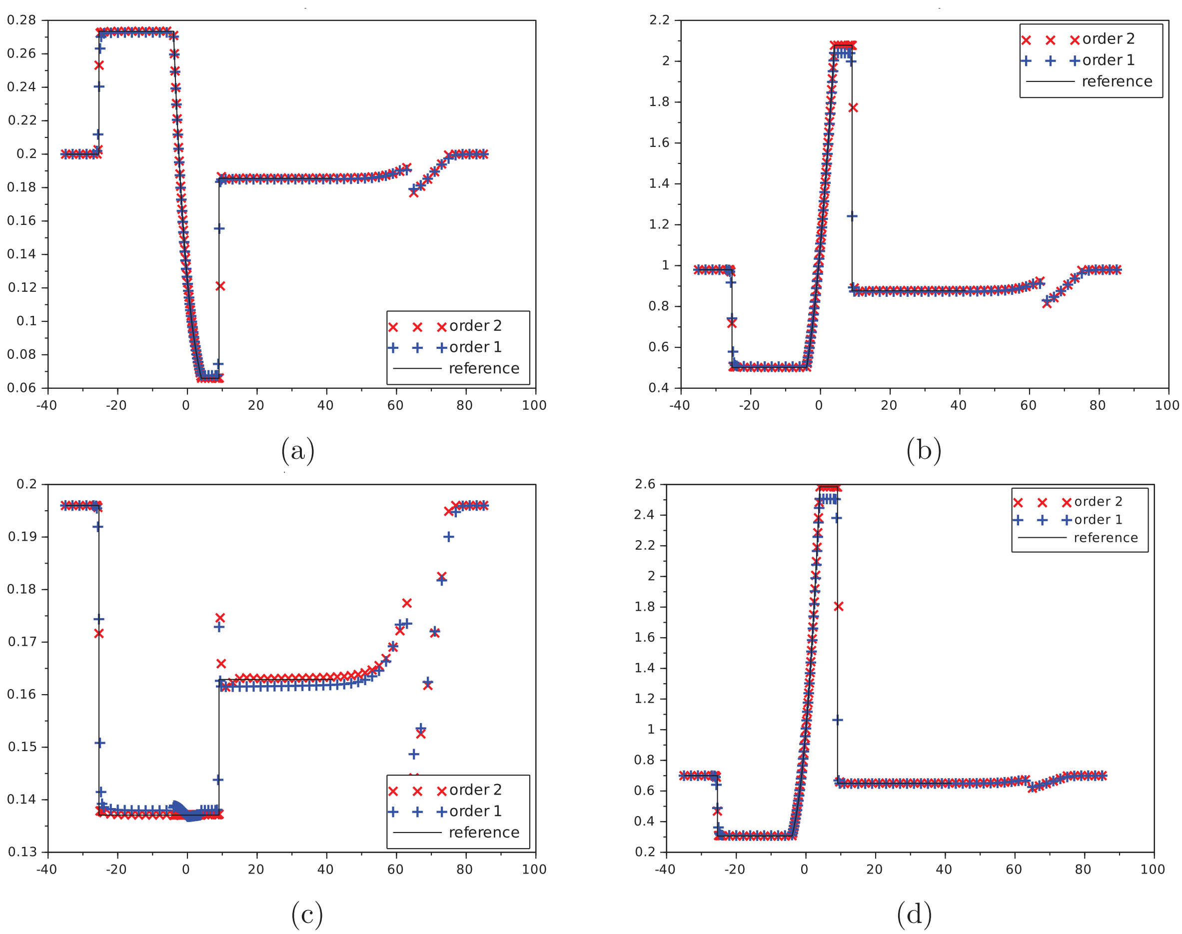

FIGURE 17. Flow over an isolated obstacle: numerical solutions obtained for $F_0 = 0.7$, $\delta x = 0.1$ at $T = 30$. (a) Height ρ. (b) Velocity u. (c) Discharge ρu. (d) Froude number.

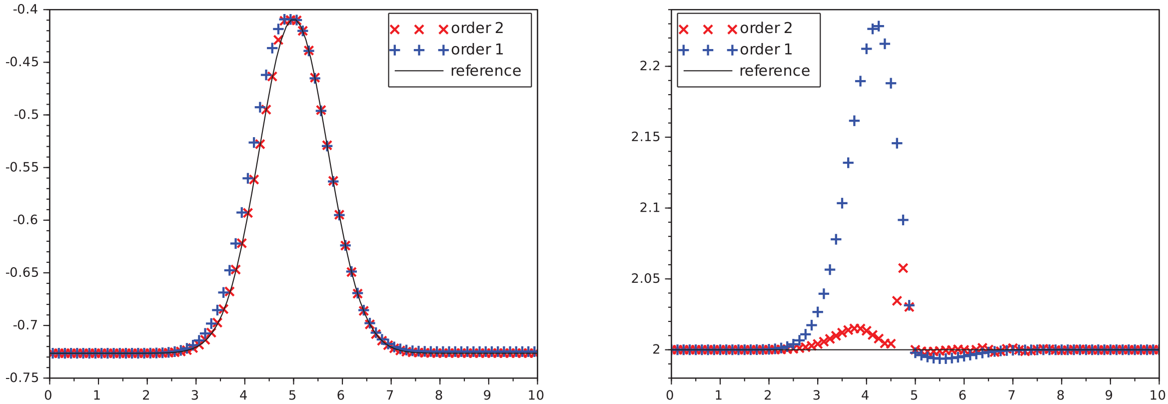

(a) (b)

FIGURE 18. Test 1 from [19]: numerical solutions obtained for $\delta x = 0.125$ and $t = 100$. (a) Free surface $\rho + z$. (b) Discharge ρu.

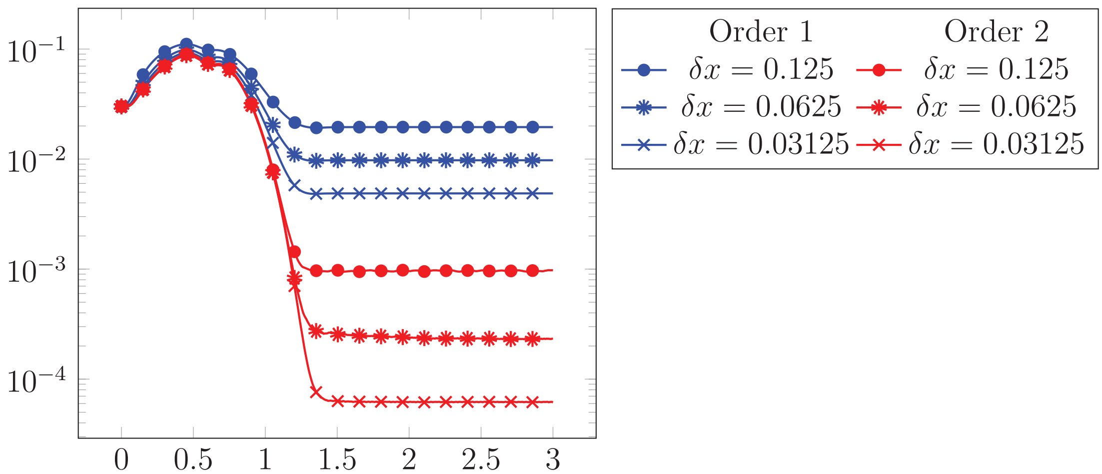

FIGURE 19. Test 1 from [19]: time evolution of the L^1-norm $\|\rho - \rho_{eq}\|_{L^1}$ of the difference between the numerical solution and the equilibrium solution.

discretisation. Due to the presence of the shock and the limitation procedure, the second order version of the scheme does not actually reach second order in this case, but it allows to increase accuracy. Figure 21 can be directly compared to Figure 2.23(h) to 2.27(h), Section 2.2.2.2 of [23].

3.4. Wet/dry fronts in a nonflat bassin

We consider in this Section a test case proposed by [28] (see also [5, 19]). The flow is governed by Shallow-Water equations ($\gamma = 2$). The computational domain is $[0, 25]$ and the gravity is $g = 9.8$. The bottom topography is defined by

$$z(x) = \begin{cases} -13, & \text{if } 25/3 < x < 25/2, \\ -14, & \text{otherwise.} \end{cases}$$

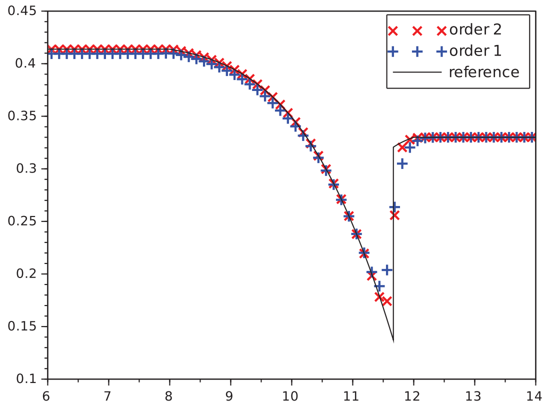

(a)

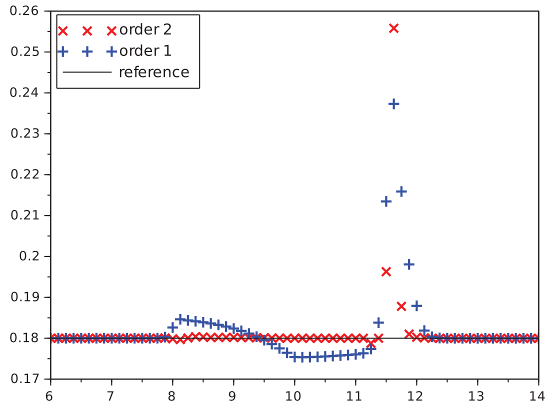

(b)

FIGURE 20. Test 2 from [19]: numerical solutions obtained for $\delta x = 0.125$ and $t = 200$. (a) Free surface $\rho + z$. (b) Discharge ρu.

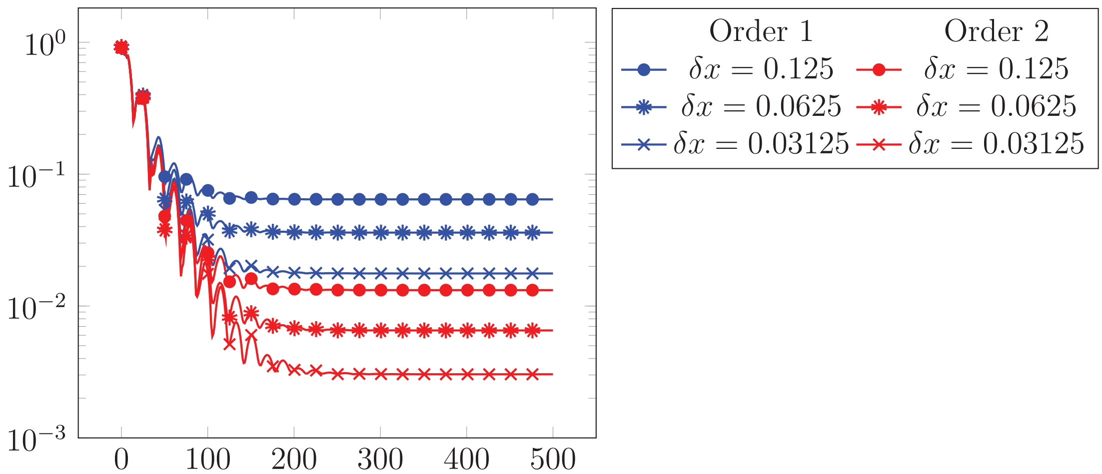

FIGURE 21. Test 2 from [19]: time evolution of the L^1-norm $\|\rho - \rho_{eq}\|_{L^1}$ of the difference between the numerical solution and the equilibrium solution.

With $q = \rho u$, the initial data are given by

$$\rho(x) = -z(x) - 4, \qquad \text{and} \qquad q(x) = \begin{cases} -350, & \text{if } x \leqslant 50/3, \\ 350, & \text{if } x > 50/3. \end{cases}$$

We use $\delta x = 5 \times 10^{-3}$ and $C_{\delta t} = 0.4$. The numerical solution obtained with our schemes are presented in Figure 22 (for the first order scheme) and in Figure 23 (for the second order scheme) at different times $t = 0.05$, $t = 0.25$ and $t = 0.45$. Two rarefaction waves propagate in opposite directions creating a dry bed. The schemes capture correctly the generation and propagation of the wet-dry fronts (even when the wave propagates over the step). The results on Figures 22 and 23 can be directly compared to Figures 17 and 18 of [28], Figure 15 of [19] or Figure 3.12 of [5].

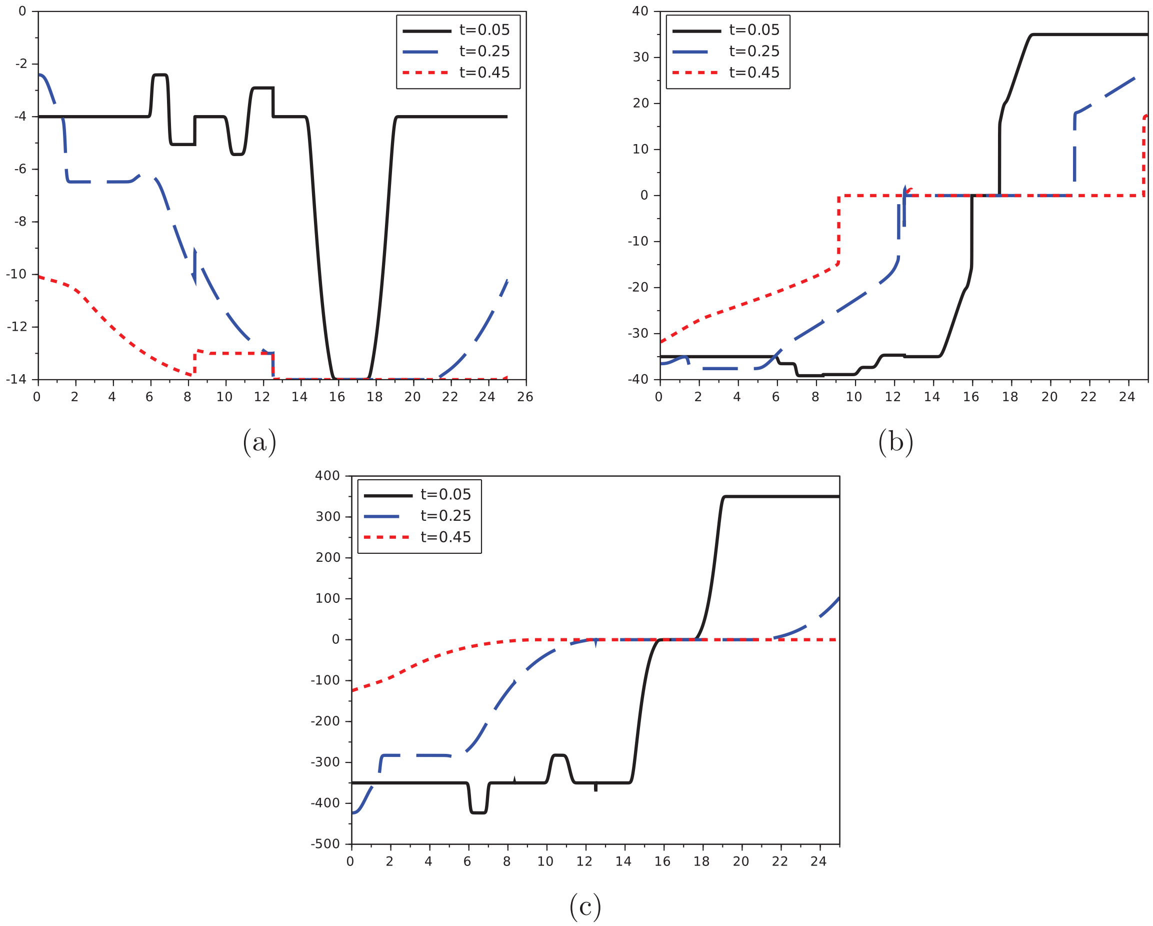

FIGURE 22. Wet/dry fronts in a nonflat bassin: numerical solutions obtained with the first order scheme, $\delta x = 0.005$. (a) Free surface $\rho + z$. (b) Velocity u. (c) Discharge ρu.

3.5. Thacker test: oscillation in a 2D-paraboloid

In this Section, we consider the 2D problem of a free surface oscillating in a paraboloid [23, 24, 60]. The flow is governed by Shallow-Water equations ($\gamma = 2$).

Restricting the discussion to Cartesian grids, it is straightforward to expand our approach to higher dimensions, as the discretization can be easily interpreted through the MAC framework. We refer the interested reader to Section 4 of [35] for a complete description of the scheme in 2D including the second order version in the absence of source term. Taking the source term into account does not pose any particular difficulty compared to what was described in 1D. As for the MUSCL reconstruction, the hydrostatic reconstruction is applied either only on the rows or only on the columns of the numerical density, depending on the considered direction x or y and it works exactly as in 1D.

The computational domain is $[-2, 2] \times [-2, 2]$. The topography is given by

$$z(x, y) = \frac{1}{2}(x^2 + y^2 - 1).$$

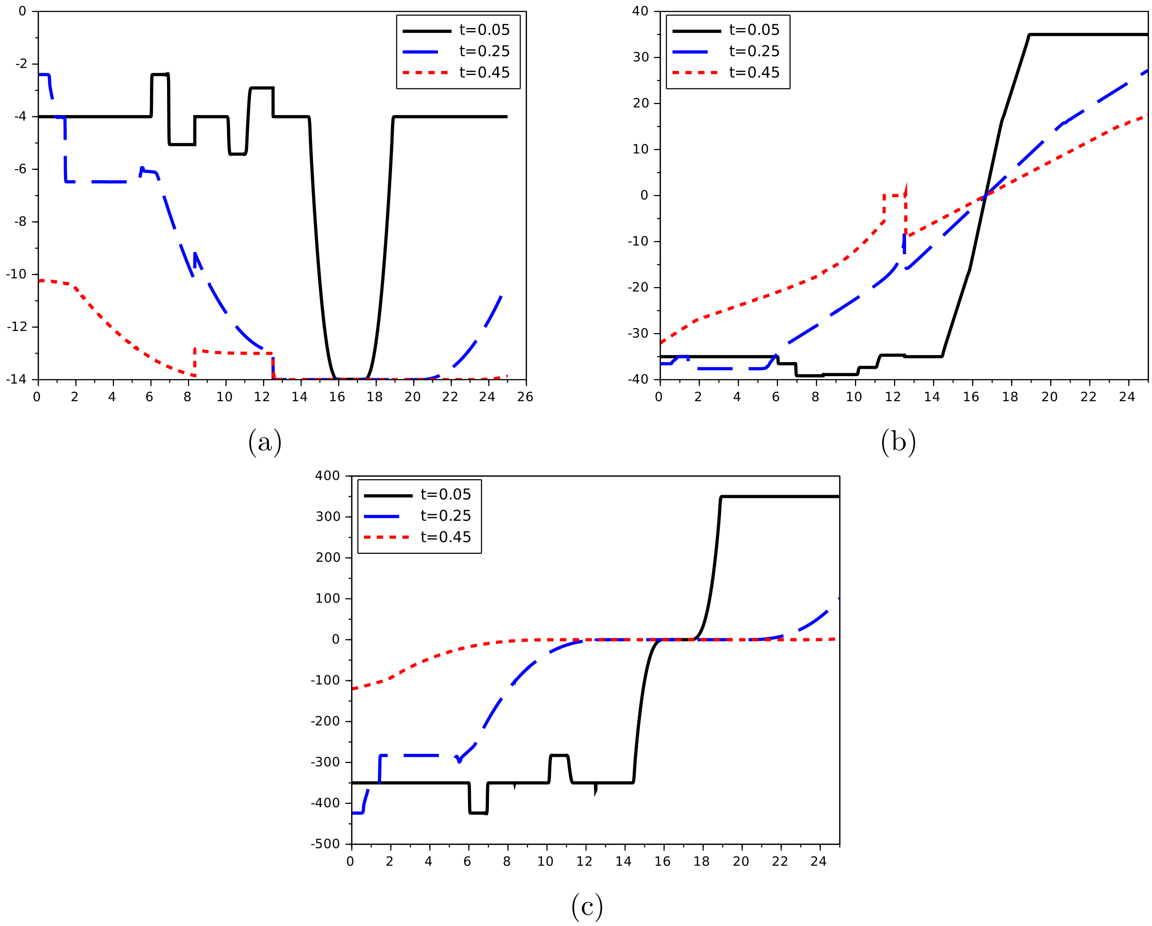

FIGURE 23. Wet/dry fronts in a nonflat bassin: numerical solutions obtained with the second order scheme, $\delta x = 0.005$. (a) Free surface $\rho + z$. (b) Velocity u. (c) Discharge ρu.

The initial data are given by

$$\rho(x, y) = \big(0.125 * (4x - 1) - z(x, y)\big)\mathbb{1}_{(x-0.5)^2+y^2<1},$$
$$u(x, y) = \begin{pmatrix} 0 \\ 0.5 \end{pmatrix} \times \mathbb{1}_{(x-0.5)^2+y^2<1}.$$

This is a planar free surface with a non-vanishing initial velocity. The solution is exactly known; it is given by

$$\begin{cases} \rho(t, x, y) = \Big(0.125\big(4x\cos(t) + 4y\sin(t) - 1\big) - z(x, y)\Big)\mathbb{1}_{(x-0.5\cos(t))^2+(y-0.5\sin(t))^2<1}, \\ u(t, x, y) = \dfrac{1}{2}\begin{pmatrix} -\sin(t) \\ \cos(t) \end{pmatrix}. \end{cases}$$

The solution is 2π-periodic with respect to the time variable. The free surface remains planar in time with a moving circular wet/dry transition line. The numerical results obtained with the first and second order schemes are presented in Figures 24 and 25. For this test case, the time step is defined by

$$\delta t = 0.2 \min\big(\delta x, \delta y\big).$$

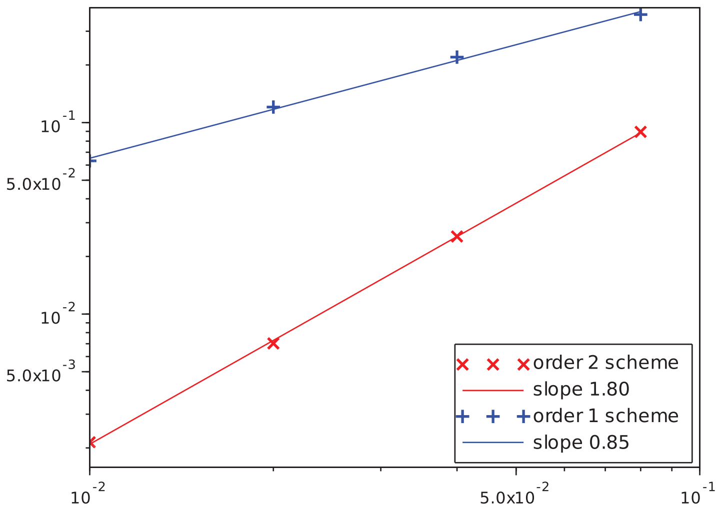

FIGURE 24. 2D Thacker test: discrete error in L^1-norm as a function of the mesh size (1st and 2nd order schemes).

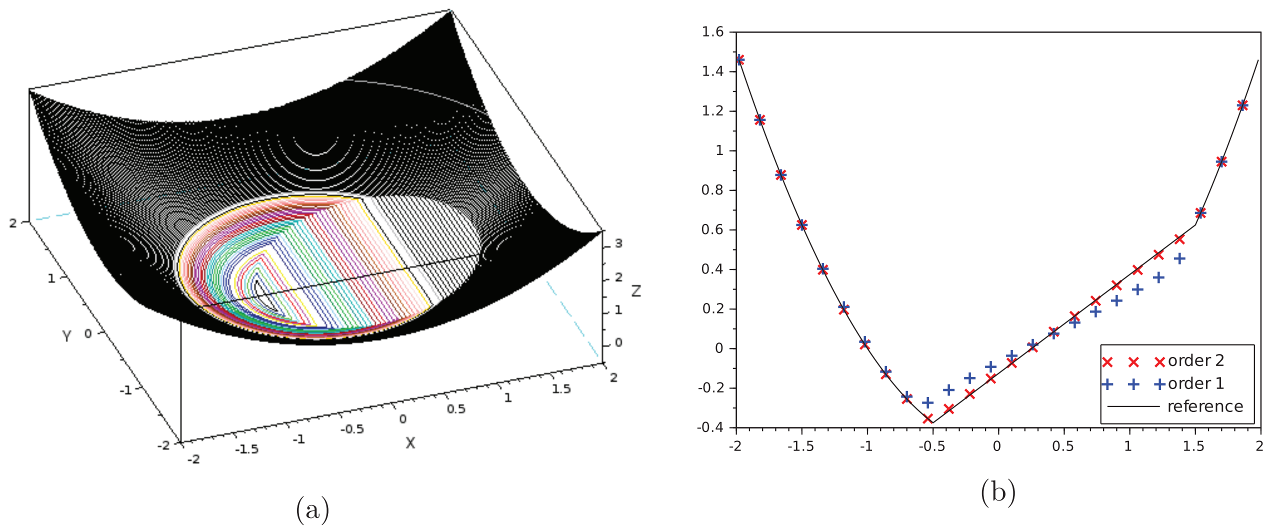

FIGURE 25. 2D Thacker test: numerical solution obtained with $\delta x = \delta y = 0.01$ using the 2nd order scheme (left) and comparison of a cutline with the first order scheme. (a) Contour lines of the free surface. (b) Cutline $y = 0$ of the free surface.

Figure 24 shows the discrete error in L^1-norm at time $T = 4\pi$ as a function of the mesh size. As expected, we observe that the MUSCL rescontruction procedure reaches higher accuracy (1.8 convergence order). The approximate solutions obtained at $T = 4\pi$ with $\delta x = 0.01$ and $\delta y = 0.01$ are presented in Figure 25. At the left, in Figure 25a, we provide the contour lines of the free surface. We clearly observe the circular shoreline and the planar free surface. In Figure 25b, we provide a cutline along the axis $y = 0$ and we compare the results obtained with the first or second order scheme with the reference exact solution.

Acknowledgements

We thank Nicolas Seguin for having encouraged us at pushing the development of our numerical method towards this direction. We are also gratefully indebted to Olivier Delestre and Thomas Rey for their advice about the numerical simulations of the paper.

References

[1] A. Arakawa and V.R. Lamb, Computational design of the basic dynamical processes of the UCLA general circulation model. *Methods Comput. Phys.: Adv. Res. Appl.* **17** (1977) 173–265.

[2] A. Arakawa and V.R. Lamb, A potential enstrophy and energy conserving scheme for the shallow water equations. *Mon. Weather Rev.* **109** (1981) 18–36.

[3] E. Audusse, F. Bouchut, M.-O. Bristeau, R. Klein and B. Perthame, A fast and stable well-balanced scheme with hydrostatic reconstruction for shallow water flows. *SIAM J. Sci. Comput.* **25** (2004) 2050–2065.

[4] E. Audusse, F. Bouchut and M.-O. Bristeau, A well-balanced positivity preserving "second-order" scheme for shallow water flows on unstructured meshes. *J. Comput. Phys.* **206** (2005) 311–333.

[5] E. Audusse, C. Chalons and P. Ung, A simple well-balanced and positive numerical scheme for the shallow-water system. *Commun. Math. Sci.* **13** (2015) 1317–1332.

[6] E. Audusse, F. Bouchut, M.-O. Bristeau and J. Sainte-Marie, Kinetic entropy inequality and hydrostatic reconstruction scheme for the Saint-Venant system. *Math. Comput.* **85** (2016) 2815–2837.

[7] D. Benson, Computational methods in lagrangian and eulerian hydrocodes. *Comput. Methods Appl. Mech. Eng.* **99** (1992) 235–394.

[8] M.V.A. Bermudez, Upwind methods for hyperbolic conservation laws with source terms. *Comput. Fluids* **23** (1994) 1049–1071.

[9] O. Bernard, M. Bestard, T. Goudon, L. Meyer, S. Minjeaud, F. Noisette and B. Polizzi, *Numerical schemes for mixture theory models with filling constraint: application to biofilm ecosystems*, Technical report, Univ. Côte d'Azur, CNRS, Inria, 2023. CEMRACS (2022).

[10] F. Berthelin, T. Goudon and S. Minjeaud, Consistency analysis of a 1D finite volume scheme for barotropic Euler models. In *Finite volumes for complex applications VII. Methods and theoretical aspects*, Vol. 77 of *Springer Proc. Math. Stat.* Springer, Cham (2014) 97–105.

[11] F. Berthelin, T. Goudon and S. Minjeaud, Kinetic schemes on staggered grids for barotropic Euler models: entropy-stability analysis. *Math. Comput.* **84** (2015) 2221–2262.

[12] F. Berthelin, T. Goudon and S. Minjeaud, Multifluid flows: a kinetic approach. *J. Sci. Comput.* **66** (2016) 792–824.

[13] C. Berthon, A. Duran, F. Foucher, K. Saleh and J. de Dieu Zabsonré, Improvement of the hydrostatic reconstruction scheme to get fully discrete entropy inequalities. *J. Sci. Comput.* **80** (2019) 924–956.

[14] R. Botchorishvili, B. Perthame and A. Vasseur, Equilibrium schemes for scalar conservation laws with stiff sources. *Math. Comput.* **72** (2003) 131–157.

[15] F. Bouchut, Nonlinear Stability of Finite Volume Methods for Hyperbolic Conservation Laws and Well-balanced Schemes for Sources. Frontiers in Mathematics, Birkhäuser (2004).

[16] `CALIF3S`, A software components library for the computation of reactive turbulent flows.

[17] P. Cargo and A.-Y. LeRoux, Un schéma équilibre adapté au modèle d'atmosphère avec termes de gravité. *C. R. Acad. Sci. Paris Sér. I Math.* **318** (1994) 73–76.

[18] M. Castro, A. Milanes and C. Pares, Well-balanced numerical schemes based on a generalized hydrostatic reconstruction technique. *Math. Models Methods Appl. Sci.* **17** (2007) 2055–2113.

[19] M.J. Castro, A. Pardo, C. Parés and E.F. Toro, On some fast well-balanced first order solvers for nonconservative systems. *Math. Comput.* **79** (2010) 1427–1472.

[20] F. Coron and B. Perthame, Numerical passage from kinetic to fluid equations. *SIAM J. Numer. Anal.* **28** (1991) 26–42.

[21] C. Dafermos, Hyperbolic conserrvation laws in continuum physics, 3rd edition. In Vol. 325 of *Grundlehren der Mathematischen Wissenschaften.* Springer, 2010.

[22] G. Dakin, B. Després and S. Jaouen, High-order staggered schemes for compressible hydrodynamics weak consistency and numerical validation. *J. Comput. Phys.* **376** (2019) 339–364.

[23] O. Delestre, *Simulation du ruissellement d'eau de pluie sur des surfaces agricoles.* Ph.D. thesis, Université d'Orléans (2010).

[24] O. Delestre, C. Lucas, P.-A. Ksinant, F. Darboux, C. Laguerre, T.-N.-T. Vo, F. James and S. Cordier, SWASHES: a compilation of shallow water analytic solutions for hydraulic and environmental studies. *Int. J. Numer. Methods in Fluids* **72** (2013) 269–300.

[25] S.M. Deshpande, Kinetic theory based new upwind methods for inviscid compressible flows. In: *AIAA 24th Aerospace Science Meeting, Jan 6–9, 1986, Nevada, USA.* AIAA paper (1986) 86–0275.

[26] S.M. Deshpande, *On the Maxwellian distribution, symmetric form and entropy conservation for the Euler equations.* Technical report, NASA Langley Research Centre, Hampton, VA (1986). NASA TP2613.

[27] D. Doyen and P.H. Gunawan, An explicit staggered finite volume scheme for the shallow water equations. In: *Finite Volumes for Complex Applications VII-Methods and Theoretical Aspects*, Vol. 77 of *Springer Proceedings in Mathematics & Statistics.* Springer (2014).

[28] T. Gallouët, J.-M. Hérard and N. Seguin, Some approximate Godunov schemes to compute shallow water equations with topography. *Comput. Fluids* **32** (2003) 479–513.

[29] T. Gallouët, R. Herbin and J.-C. Latché, Lax–wendroff consistency of finite volume schemes for systems of non linear conservation laws: extension to staggered schemes. *SeMA* **79** (2022) 333–354.

[30] L. Gastaldo, R. Herbin, W. Kheriji, C. Lapuerta and J.-C. Latché, Staggered discretizations, pressure correction schemes and all speed barotropic flows. In Vol. 4 *Finite Volumes for Complex Applications VI, Problems and Perspectives, Prague, Czech Republic* (2011) 839–855.

[31] L. Gastaldo, R. Herbin, J.-C. Latché and N. Therme, A MUSCL-type segregated-explicit staggered scheme for the Euler equations. *Comput. Fluids* **175** (2018) 91–110.

[32] E. Godlewski and P.-A. Raviart, Numerical approximation of hyperbolic systems of conservation laws. In Vol. 118 of *Applied Mathematical Sciences.* Springer, New-York (1996).

[33] L. Gosse, Computing qualitatively correct approximations of balance laws. In Vol. 2 of *SIMAI Springer Series.* Spinger (2013).

[34] T. Goudon, J. Llobell and S. Minjeaud, An asymptotic preserving scheme on staggered grids for the barotropic Euler system in low Mach regimes. *Numer. Methods PDE* **36** (2020) 1098–1128.

[35] T. Goudon, J. Llobell and S. Minjeaud, An explicit MUSCL scheme on staggered grids with kinetic-like fluxes for the barotropic and full Euler system. *Commun. Comput. Phys.* **27** (2020) 672–724.

[36] T. Goudon, J. Llobell and S. Minjeaud, An explicit finite volume scheme on staggered grids for the Euler equations: unstructured meshes, stability analysis, and energy conservation. *Int. J. Numer. Methods Fluids* **94** (2022) 76–119.

[37] J.M. Greenberg and A.-Y. Leroux, A well-balanced scheme for the numerical processing of source terms in hyperbolic equations. *SIAM J. Numer. Anal.* **33** (1996) 1–16.

[38] H. Guillard and C. Viozat, On the behavior of upwind schemes in the low Mach number limit. *Comput. Fluids* **28** (1999) 63–86.

[39] H. Guillard and B. Nkonga, Chapter 8 – on the behaviour of upwind schemes in the low mach number limit: A review. In Vol. 18 of *Handbook of Numerical Analysis*, edited by R. Abgrall and C.-W. Shu. *Handbook of Numerical Methods for Hyperbolic Problems.* Elsevier (2017) 203–231.

[40] F.H. Harlow and J.E. Welch, Numerical calculation of time-dependent viscous incompressible flow of fluid with free surface. *Phys. Fluids* **8** (1965) 2182–2189.

[41] F.H. Harlow and A.A. Amsden, Numerical calculation of almost incompressible flow. *J. Comput. Phys.* **3** (1968) 80–93.

[42] F.H. Harlow and A.A. Amsden, A numerical fluid dynamics calculation method for all flow speeds. *J. Comput. Phys.* **8** (1971) 197–213.

[43] R. Herbin, W. Kheriji and J.-C. Latché, Staggered schemes for all speed flows. *ESAIM: Proc.* **35** (2012) 122–150.

[44] R. Herbin, J.-C. Latché and T.T. Nguyen, Explicit staggered schemes for the compressible Euler equations. In *Applied mathematics in Savoie—AMIS 2012: Multiphase flow in industrial and environmental engineering*, Vol. 40 of *ESAIM Proc.*, EDP Sciences (2013) 83–102.

[45] R. Herbin, J.-C. Latché and T.T. Nguyen, Consistent segregated staggered schemes with explicit steps for the isentropic and full Euler equations. *ESAIM:M2AN* **52** (2018) 893–944.

[46] R. Herbin, J.-C. Latché, S. Minjeaud and N. Therme, Conservativity and weak consistency of a class of staggered finite volume methods for the Euler equations. *Math. Comput.* **90** (2021) 1155–1177.

[47] R. Herbin, J.-C. Latché and K. Saleh, Low Mach number limit of some staggered schemes for compressible barotropic flows. *Math. Comput.* **90** (2021) 1039–1087.

[48] D.D. Houghton and A. Kasahara, Nonlinear shallow fluid flow over an isolated ridge. *NCAR Manuscript* **259a** (1967).

[49] S. Kaniel and J. Falcovitz, Approximation of the hydrodynamic equations by a transport process, edited by R. Rautman. In: *Proceedings of IUTAM Symposium on Approximation Methods for Navier-Stokes Problems*, Vol. 771 of *Lecture Notes in Math.* Springer-Verlag (1980).

[50] W. Kheriji, R. Herbin and J.-C. Latché, Pressure correction staggered schemes for barotropic one-phase and two-phase flows. *Comput. Fluids* **88** (2013) 524–542.

[51] C. Klingenberg, G. Puppo and M. Semplice, Arbitrary order finite volume well-balanced schemes for the Euler equations with gravity. *SIAM J. Sci. Comput.* **41** (2019) A695–A721.

[52] F. Lespagnol and G. Dakin, High order accurate schemes for Euler and Navier-Stokes equations on staggered Cartesian grids. *J. Comput. Phys.* **410** (2020) 109314.

[53] R. LeVeque, Balancing source terms and flux gradients in high-resolution godunov methods: The quasi-steady wave-propagation algorithm. *J. Comput. Phys.* **146** (1998) 346–365.

[54] R.J. LeVeque, *Finite volume methods for hyperbolic problems.* Cambridge Texts in Applied Mathematics, Cambridge University Press, Cambridge (2002).

[55] V. Michel-Dansac, C. Berthon, S. Clain and F. Foucher, A well-balanced scheme for the shallow-water equations with topography. *Comput. Math. Appl.* **72** (2016) 568–593.

[56] B. Perthame, Second order Boltzmann schemes for compressible Euler equations in one and two space dimension. *SIAM J. Numer. Anal.* **29** (1992) 1–19.

[57] B. Perthame, Kinetic Formulation of Conservation Laws. Oxford Lecture Series in Math. and its Appl. Oxford University Press (2003).

[58] B. Polizzi, O. Bernard and M. Ribot, A time-space model for the growth of microalgae biofilms for biofuel production. *J. Theor. Biol.* **432** (2017) 55–79.

[59] G. Stelling and S. Duinmeijer, A staggered conservative scheme for every Froude number in rapidly varied shallow water flows. *Int. J. Numer. Methods Fluids* **43** (2003) 1329–1354.

[60] W.C. Thacker, Some exact solutions to the nonlinear shallow-water wave equations. *J. Fluid Mech.* **107** (1981) 499–508.

[61] E.F. Toro, Riemann Solvers and Numerical Methods for Fluid Dynamics, 3rd edition. Springer-Verlag, Berlin (2009).

[62] D.R. van der Heul, C. Vuik and P. Wesseling, A conservative pressure-correction method for flow at all speeds. *Comput. Fluids* **32** (2003) 1113–1132.

[63] B. van Leer, Towards the ultimate conservative difference scheme. V. A second-order sequel to Godunov's method. *J. Comput. Phys.* **135** (1997) 227–248.

[64] B. van't Hof and A.E.P. Veldman, Mass, momentum and energy conserving (MaMEC) discretizations on general grids for the compressible Euler and shallow water equations. *J. Comput. Phys.* **231** (2012) 4723–4744.

[65] J. VonNeumann and R.D. Richtmyer, A method for the numerical calculation of hydrodynamic shocks. *J. Appl. Phys.* **21** (1950) 232–237.

[66] I. Wenneker, A. Segal and P. Wesseling, A Mach-uniform unstructured staggered grid method. *Int. J. Numer. Methods Fluids* **40** (2002) 1209–1235.

[67] I. Wenneker, A. Segal and P. Wesseling, Conservation properties of a new unstructured staggered scheme. *Comput. Fluids* **32** (2003) 139–147.

[68] P. Wesseling, Principles of computational fluid dynamics. In Vol. 29 of *Springer Series in Computational Mathematics.* Springer (2001).

[69] P. Woodward and P. Colella, The numerical simulation of two-dimensional fluid flow with strong shocks. *J. Comput. Phys.* **54** (1984) 115–173.